AFGL-TR-82-0075

$\textcircled{12}$

AIRGLOW IMAGING STUDIES

OF NATURAL AND ARTIFICIALLY INDUCED

IONOSPHERIC DISTURBANCES

Michael Mendillo, Jeffrey Baumgardner and Harlan Spence

Department of Astronomy
Boston University
725 Commonwealth Avenue
Boston, Massachusetts   02215

Approved for public release; distribution unlimited.

AIR FORCE GEOPHYSICS LABORATORY
AIR FORCE SYSTEMS COMMAND
UNITED STATES AIR FORCE
HANSCOM AFB, MASSACHUSETTS 01731

DTIC
ELECTE
MAY 1 2 1982

E

82   05-12   00

Qualified requestors may obtain additional copies from the
Defense Technical Information Center. All others should
apply to the National Technical Information Service.

REPORT DOCUMENTATION PAGE		READ INSTRUCTIONS BEFORE COMPLETING FORM
1. REPORT NUMBER AFGL-TR-82-0075	2. GOVT ACCESSION NO. AD-A114 364	3. RECIPIENT'S CATALOG NUMBER
4. TITLE (and Subtitle) AIRGLOW IMAGING STUDIES OF NATURAL AND ARTIFICIALLY INDUCED IONOSPHERIC DISTURBANCES		5. TYPE OF REPORT & PERIOD COVERED Final Report 1 Oct 1979 - 30 Sept 1981
		6. PERFORMING ORG. REPORT NUMBER A.C. B.U., Ser III, No. 16
7. AUTHOR(s) Michael Mendillo Jeffrey Baumgardner Harlan Spence		8. CONTRACT OR GRANT NUMBER(s) F-19628-77-C-0270
9. PERFORMING ORGANIZATION NAME AND ADDRESS Astronomy Department, Boston University 725 Commonwealth Avenue Boston, Massachusetts 02215		10. PROGRAM ELEMENT, PROJECT, TASK AREA & WORK UNIT NUMBERS 62101 F 464304 CB
11. CONTROLLING OFFICE NAME AND ADDRESS Air Force Geophysics Laboratory Hanscom AFB, Massachusetts 01731 Contract Monitor: J.A. Klobuchar/PHY		12. REPORT DATE February 1982
		13. NUMBER OF PAGES 94
14. MONITORING AGENCY NAME & ADDRESS(if different from Controlling Office)		15. SECURITY CLASS. (of this report) Unclassified
		15a. DECLASSIFICATION DOWNGRADING SCHEDULE

16. DISTRIBUTION STATEMENT (of this Report)

Approved for public release; distribution unlimited.

17. DISTRIBUTION STATEMENT (of the abstract entered in Block 20, if different from Report)

18. SUPPLEMENTARY NOTES

19. KEY WORDS (Continue on reverse side if necessary and identify by block number)

6300Å AIRGLOW
LOW LIGHT LEVEL IMAGING
EQUATORIAL PLASMA DEPLETIONS
IONOSPHERIC HOLES

ROCKET EXHAUST EFFECTS
IONOSPHERIC IRREGULARITIES
IONOSPHERIC DISTURBANCES
MAN MADE DISTURBANCES

20. ABSTRACT (Continue on reverse side if necessary and identify by block number)

A low light level, image intensified airglow monitoring system has been developed for ground-based studies of 6300Å airglow characteristics of equatorial plasma depletions and rocket exhaust induced ionospheric holes. The system was designed for narrow band interference filters (6 Å FWHP) with interchangeable all-sky (180°) and narrow field (60°) lenses; it records images photographically using a standard 35mm camera.

DD FORM 1473 EDITION OF 1 NOV 65 IS OBSOLETE
1 JAN 73

20. cont.

The airglow system was used in two field test campaigns: (1) on Ascension Island from 24 January - 10 February 1981 to record the optical characteristics of equatorial plasma depletions and (2) near Edwards AFB to monitor the airglow signature of an ionospheric hole caused by the launch of the NOAA-C weather satellite on 23 June 1981.

In addition to the morphology features capable of being extracted directly from airglow photographs, the field test data were used to investigate various image processing techniques that could yield quantitative, photometric characteristics for the effects recorded.

The two week equatorial campaign resulted in sufficient data to study airglow depletion occurrence rates, spatial extents, alignments, drift speeds, depths and edge effects. The rocket hole data provided estimates of high altitude diffusion rates and in-situ values for photochemical reaction rates related to natural and perturbation processes.

TABLE OF CONTENTS

Accession For		
NTIS GRA&I	X	
DTIC TAB	☐	
Unannounced	☐	
Justification		
By		
Distribution/		
Availability Codes		
Dist	Avail and/or Special	
A		

DTIC
COPY
INSPECTED
3

Acknowledgements

AIRGLOW IMAGING STUDIES OF NATURAL AND
ARTIFICIALLY INDUCED IONOSPHERIC DISTURBANCES

CHAPTER 1

INTRODUCTION

During the past four years, a series of investigations of "ionospheric
variability" have focused on the variety of components that contribute to
the significant (20-25) day-to-day variations of the F-region. These
components included periodic sources (lunar tidal effects), quasi-periodic
sources (solar sector boundary effects), and the essentially random geo-
magnetic activity effects (Mendillo and Lynch, 1979; Schatten and Mendillo, 1980).
All of the above investigations were carried out using satellite radio beacon
observations of total electron content (TEC) obtained from the AFGL/AWS net-
work of TEC monitoring sites (Klobuchar, private communication). During the
final phase of this work, our emphasis was switched to a different technique
(wide-angle airglow imaging) in order to investigate two additional types of
variations found in the F-region: (1) the severe plasma depletions (or "bubbles")
that occur naturally during the post-sunset hours at equatorial locations, and
(2) the artificially-induced F-region depletions (or "ionospheric holes") that
accompany rocket exhaust injections above 200 km. While both of these phenomena
have been studied using radio techniques, airglow imaging diagnostics offer a
new and complementary approach to these problems. In addition to the usual
benefits of detailed morphology information associated with any all-sky photo-
graphic system, image processing techniques can be applied to airglow images
to yield additional, quantitative results related directly to physical and

chemical processes operating in the upper atmosphere.

In Chapter 2 of this report, we describe the low-light level airglow monitoring system developed for these studies. Chapter 3 contains a summary of the data reduction and image processing techniques applied to the observations. Two experimental campaigns were carried out to test the optical system for equatorial airglow depletion studies and rocket-induced airglow enhancement observations; results from these investigations are presented in Chapters 4 and 5.

References

Mendillo, Michael, and Francis X. Lynch, The influence of geomagnetic activity on the day-to-day variability of the ionospheric F-region, Tech. Report #79-0074, Air Force Geophysics Laboratory, Hanscom AFB, MA. 01730, 1979.

Sclatten, Kenneth H., and Michael Mendillo, Short term periodicities in ionospheric total electron content, Tech. Report #80-0096, Air Force Geophysics Laboratory, Hanscom AFB, MA. 01730, 1980.

AN ALL - SKY CAMERA SYSTEM

1. Performance Criteria

An all-sky camera system (ASCS) was originally designed to address the needs of a specific observational campaign: to monitor airglow depletions observed in the equatorial ionosphere over Ascension Island. The airglow data taken during this campaign was to be used in conjunction with other diagnostic techniques to assess the impact of equatorial plasma depletions on the NAVSTAR Satellite Navigation System.

The specific design goals of the camera system for this campaign were: (a) to record all-sky images of 6300$\overset{\bullet}{A}$ airglow emissions at brightness levels $\sim$ 50 Rayleighs; (b) to be able to distinguish features in the airglow as small as 1°; and (c) to monitor the airglow depletions in a real time mode.

Additional design goals of the system not nessarily related to the Ascension Island campaign were the ability: (d) to operate under adverse lighting conditions (twilight, moon); (e) to select different wavelength bands (e.g., 5577$\overset{o}{A}$ or 7774$\overset{o}{A}$); (f) to exchange the fisheye lens for lenses with smaller fields of view and therefore increased resolution ($\sim$ 1 min of arc); and (g) to take data suitable for subsequent photometric reduction.

2. Design Constraints

The two most important constraints in designing the all-sky camera system were cost and time - only 25 man-weeks at 20% effort were available to design, build and test the system before the system was to be used in the field.

To keep costs down the system had to be designed using easily obtainable "off the shelf" components wherever possible. The decision was made to record the data photographically rather than electronically (i.e., television system). In addition to reducing the cost, a photographic approach has considerably less bulk and complexity than a TV system and therefore would be much easier to set up in the field.

3. Design Details

3.1 Fish-eye lens

Two commonly available "fish-eye" lenses were considered for the first element in the system. The NIKKOR 8mm FL F/2.8 lens produces a 23mm diameter image covering a full hemisphere. The ROKKOR-X 16mm FL F/2.8 lens for Minolta cameras has a 40mm diameter image (the diagonal of 35mm frame) also having a field of view of 180°. The actual choice of lens was determined by other design constraints in the system.

3.2 Interference Filters

A major design problem was the use of narrow band interference filters with wide field angle objective lenses. The use of narrow band pass filters was necessary because of the comparatively weak airglow signal ($\sim$ 100 R) anticipated at Ascension Island, and a background continuum of $\sim$ 3R/A at 6300A (due to nonspectral sources, stars, etc.). A system would have to isolate a 30A wide portion of the spectrum to reduce the background to $\sim$100 R. Filters with even narrower band passes than this would be necessary if the system had to perform under adverse lighting conditions (e.g., scattered moonlight could produce $\sim$ 20R/A).

The difficulty in using interference filters to limit the band pass of an all-sky system is that the band pass of an interference filter shifts to shorter wavelengths for rays that are skew to the filter's normal (see figure 1). The severity of this shift depends on the index of refraction of the materials used to construct the filter (see figure 2).

Two possibilities for using interference filters with all-sky imaging systems were investigated. Figures 3 and 4 show the two designs considered in schematic form.

In Figure 3, the filter is placed in the diverging rays from the fish-eye lens after the rays have passed through the focus. A field lens has been added at the image plane to make the central axis of the diverging cones of light parallel to the optical axis of the system. This approach is similar to that of Mende et al. (1976). The maximum angle that any ray makes with the filter normal in this system is: $\alpha = TAN^{-1}(\frac{1}{2F})$. For either of the lenses considered above $\alpha \approx 10^{o}$. The sizes of the filters using this approach would be approximately the same as the sizes of the images formed by the fisheye lenses. Referring to Figure 5, it can be seen that the filter passband would have to be $\sim$ 40 A and centered at 6310Å, so that all the rays will pass within the 90% (normalized) transmission region of the filter. Note that in this design the rays from the edge of the field of view of the fisheye are treated the same as those from the center of the field of view (see Fig.3).

Figure 4 shows an alternate method of treating the problem. In this approach, the diverging rays from the image are collimated before passing through the filter. To ensure that all the light from the fisheye enters the collimator lens, a field lens is again employed. The focal length of the field lens is
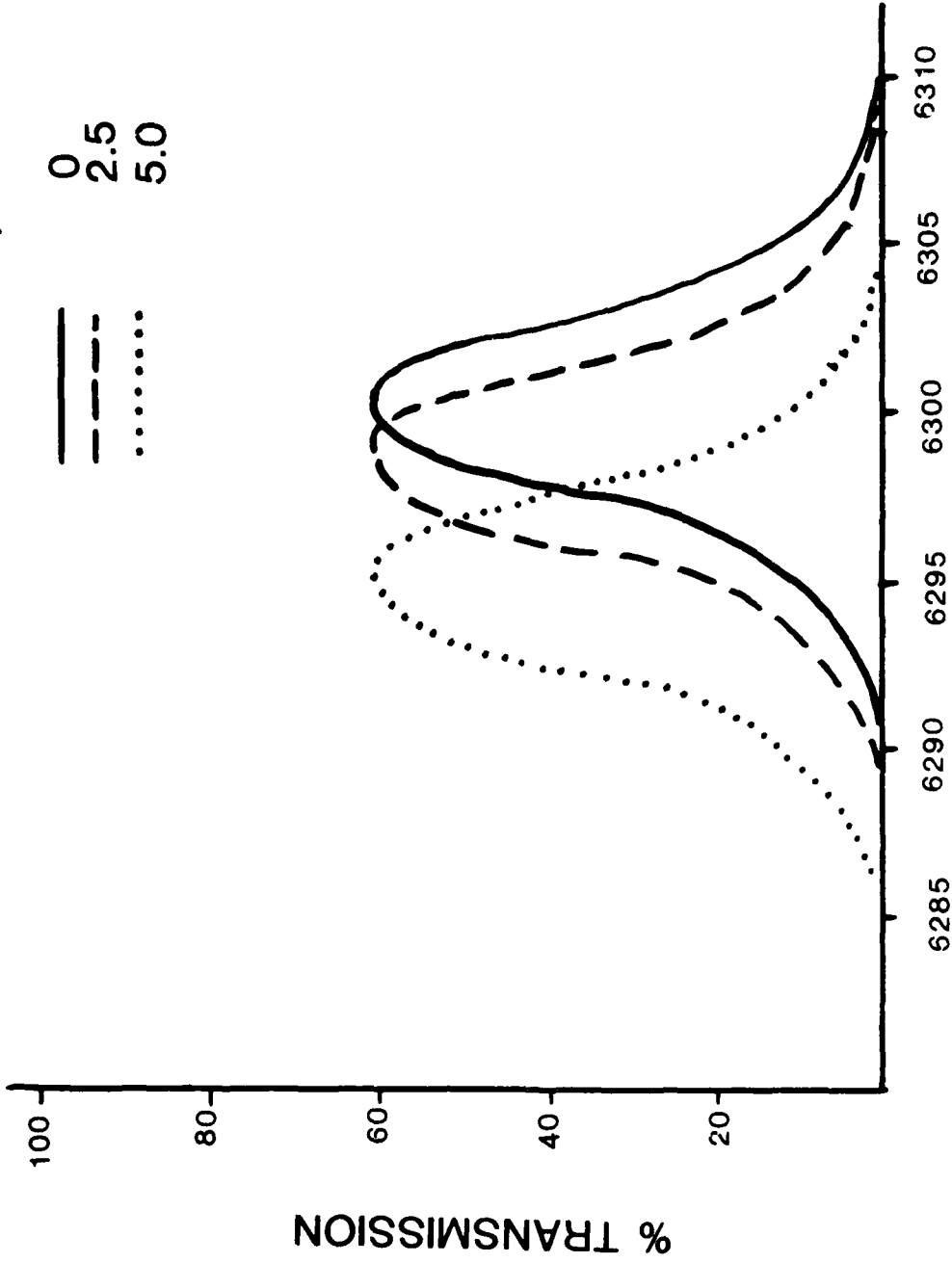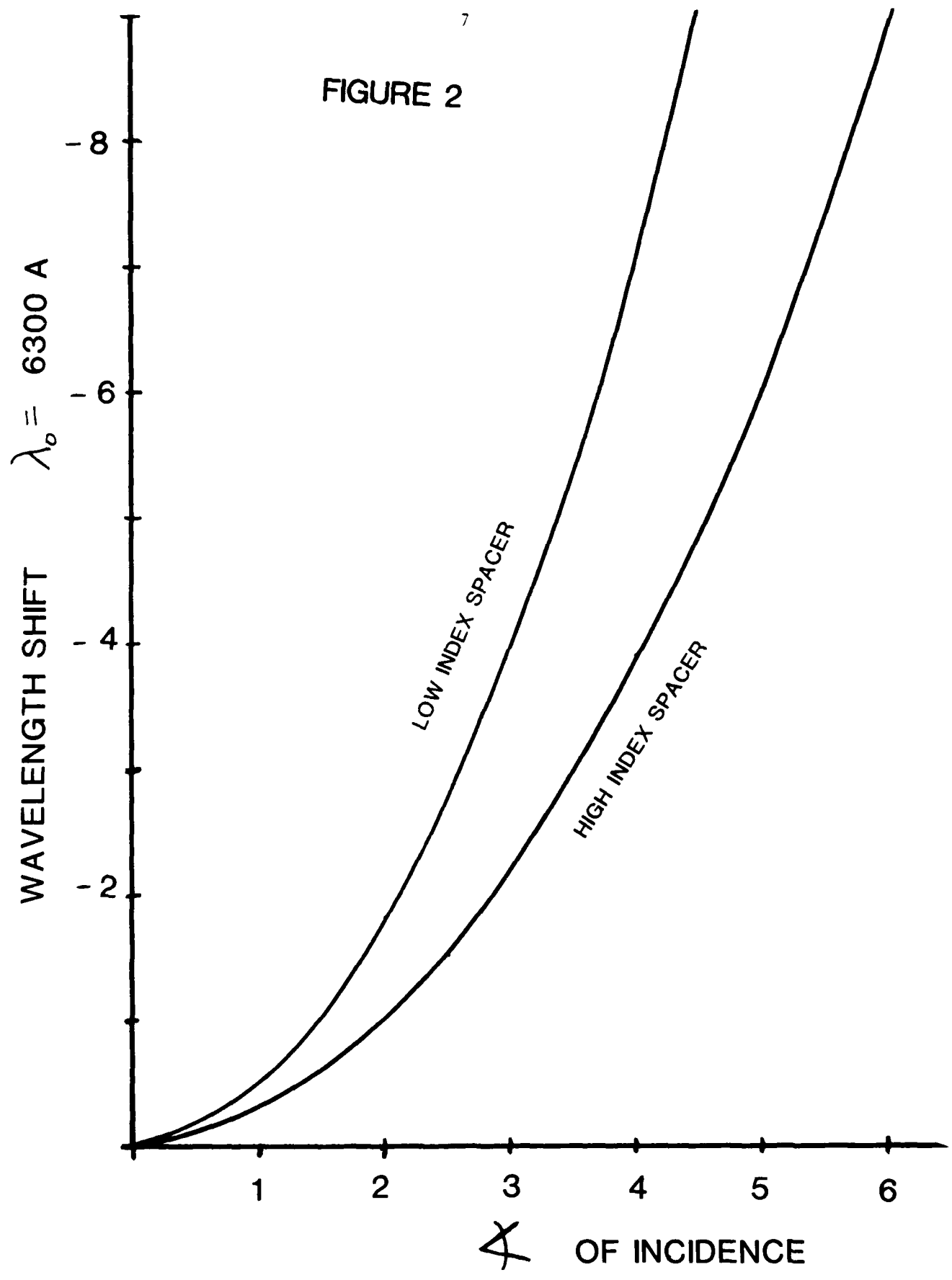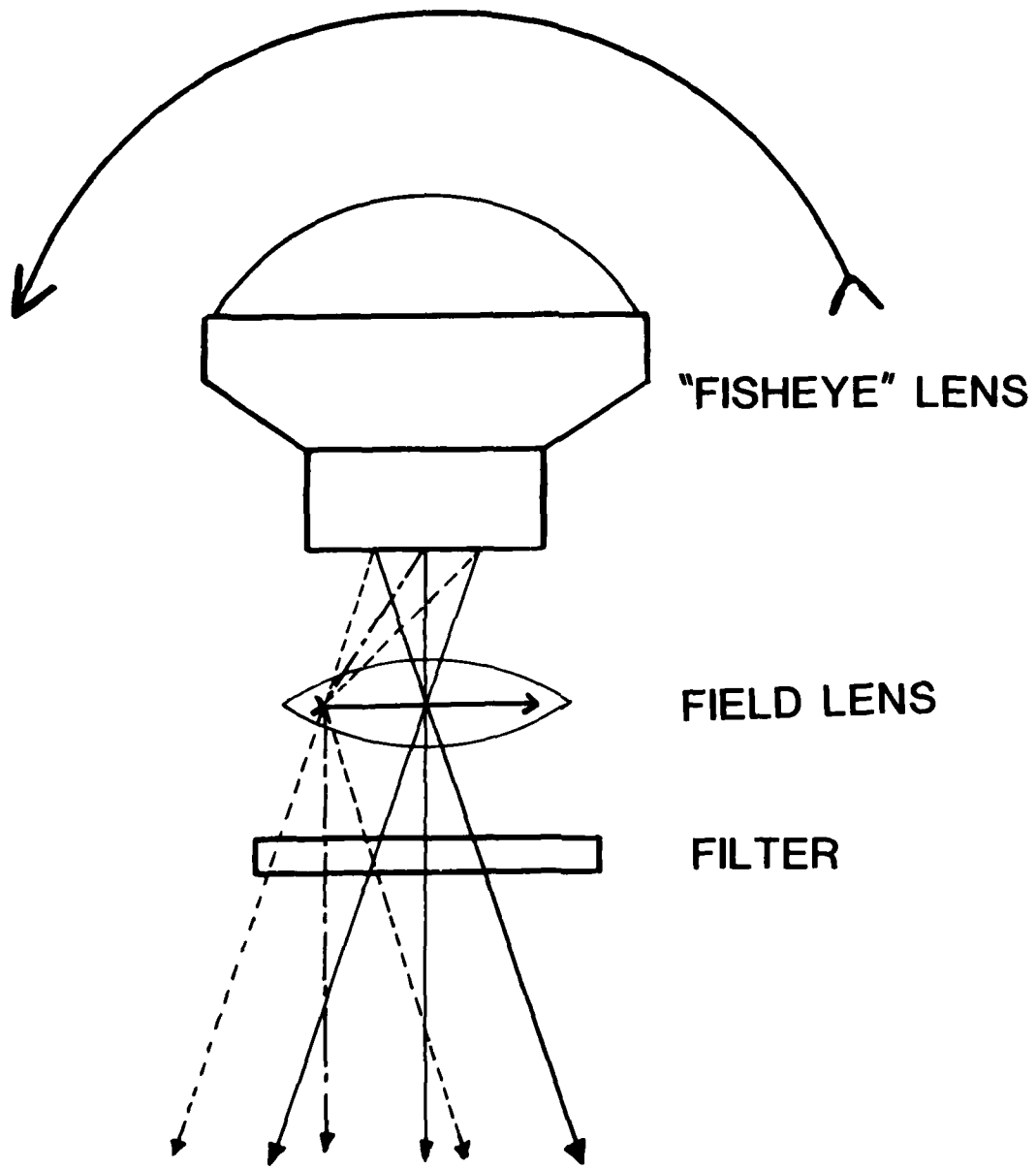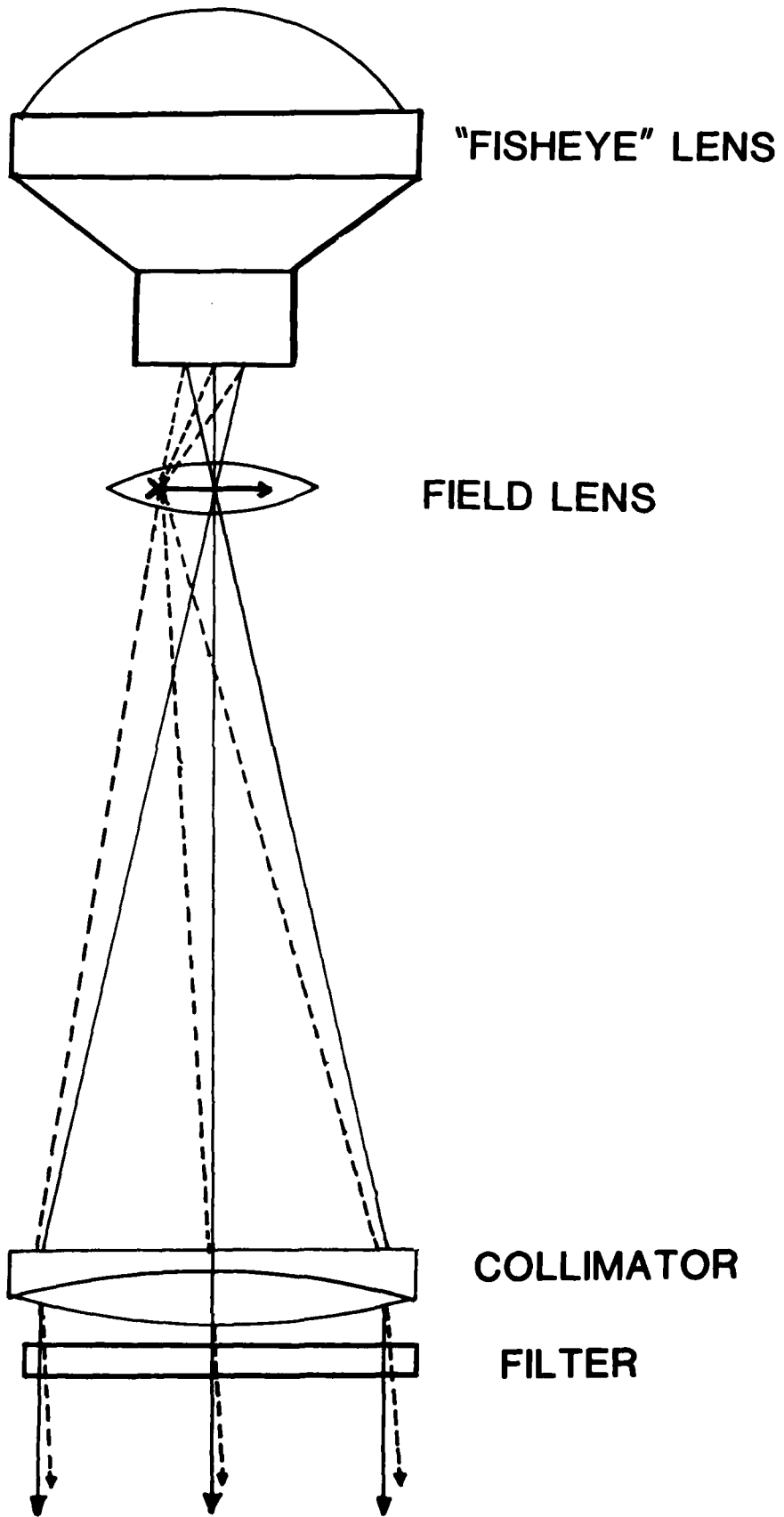
FIGURE 1

FIGURE 2

"FISHEYE" LENS

FIELD LENS

FILTER

FIGURE 3

"FISHEYE" LENS

FIELD LENS

FIGURE 4

COLLIMATOR

FILTER

FIGURE 5
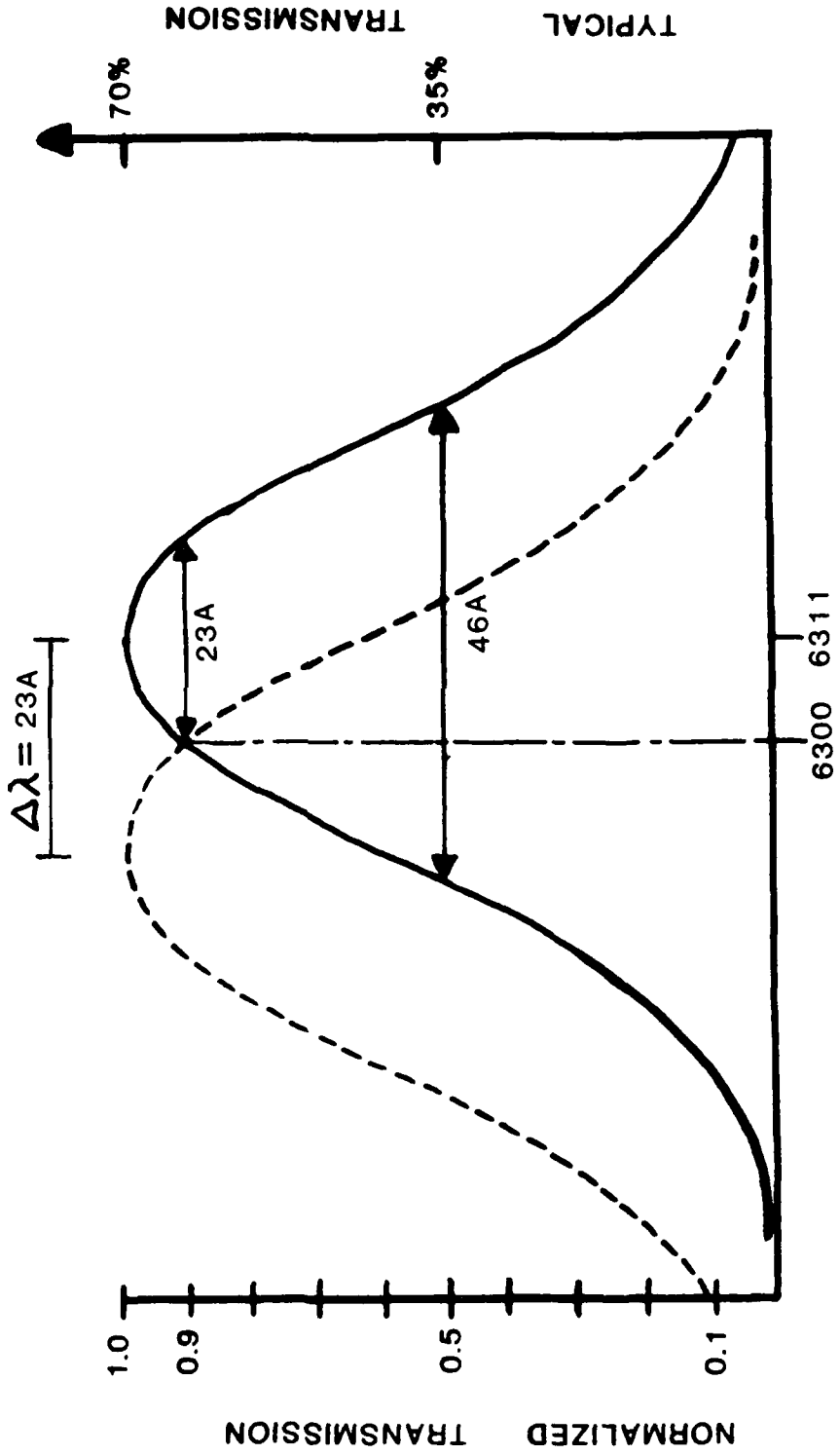
such that it images the aperture stop of the fisheye onto the filter. The filter sees a bundle of rays from the center of the field of view all parallel to the optical axis. For rays originating near the edge of the field of view, the filter sees a parallel bundle of rays whose axis makes an angle to the optical axis equal to one-half the angular size of the image as viewed from the collimator. It is obvious that this angle can be made arbitrarily small by placing the collimator far away from the image. This angle is also minimized by starting with a fisheye lens that produces a small image. In practice, however, the collimator can not be placed at great distances from the image because the diverging beam from the image gets too large. Therefore, the practical limit on the focal length of the collimator is set by how large a filter can be obtained. Without going through the extraordinary procedure of making a mosaic filter, the practical upper limit for interference filters with $\sim$ 6A passbands was found to be $\sim$ 100mm in diameter (the main constraints being cost and quality control). The selection of this filter size and the NIKKOR Fisheye lens defined the minimum passband possible for a filter. The maximum spacing between the image formed by the fisheye lens and a 100mm diameter collimator is 285 mm. To separate them more than this would allow the diverging beam to overfill the collimator. With a collimator focal length of 285 mm and an image radius of 11.5 mm, the maximum angle any ray would make with the filter normal is 2.3^{o}. Referring again to Figure 2, this angle of incidence would result in a wavelength shift of approximately 1.5A. To ensure that all of the rays pass through the filter within the 90% (normalized) transmission region, the FWHP passband of the filter would have to be at least 3A and be centered at $\sim$ 6301A (see figure 6). The center wavelength of these

FIGURE 6
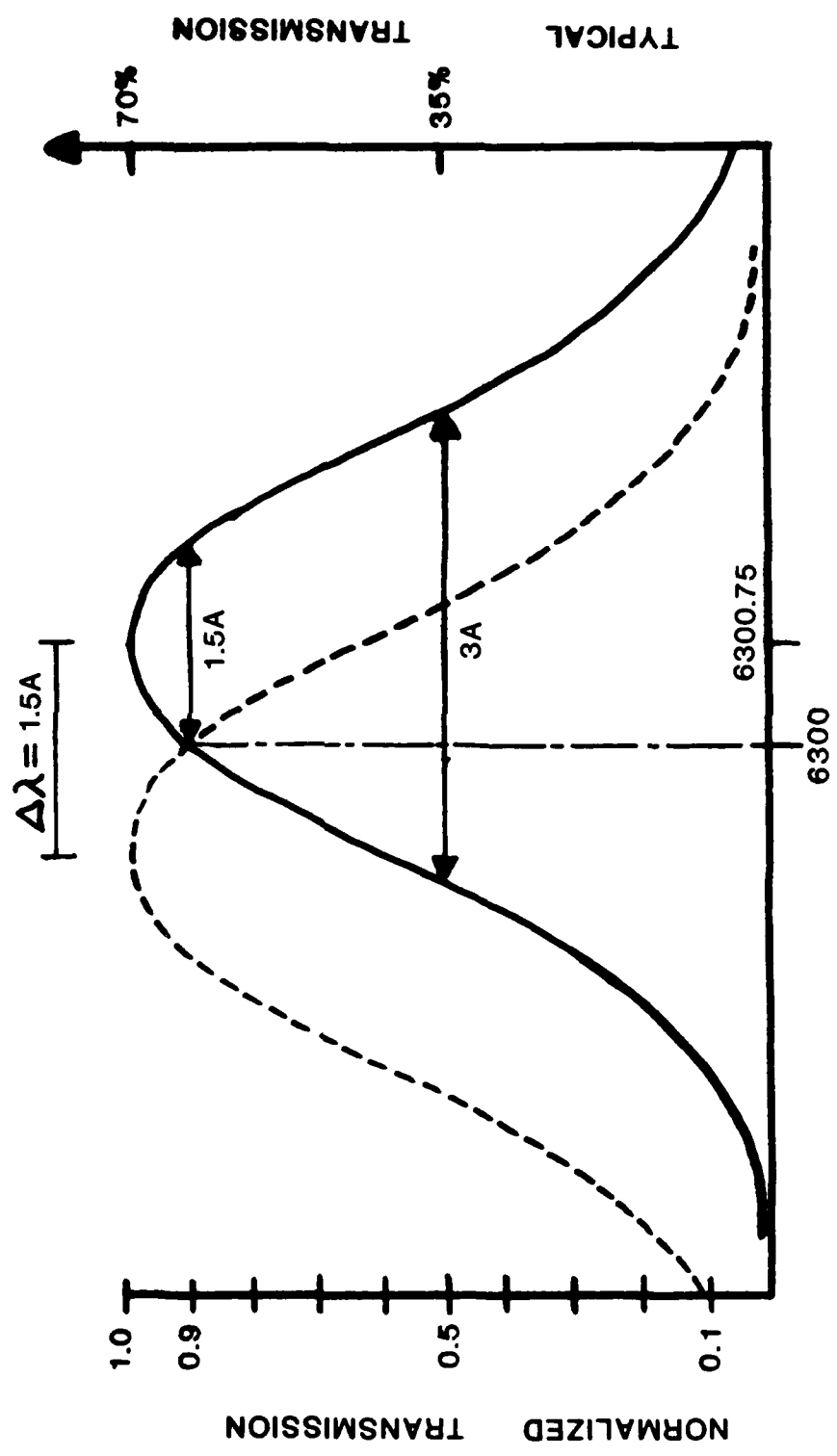
filters shift to longer wavelengths as temperature is increased with a coefficient of $\sim 0.2A/^{\circ}C$. Therefore, the filters are housed in a temperature controlled oven.

The closest match to the ideal collimator lens for the system was an ACHROMAT 88mm in diameter, 241mm focal length. This slightly shorter focal length increased the maximum angle of incidence at the filter to 2.7° and therefore, the minimum passband of the filters to be used with the system increased to 6A.

After passing through the filter, the collimated light is re-imaged by a lens identical to the collimator described above. This filtered image is the same size as the image formed by the fisheye lens and is slightly concave toward the objective lens -- a problem easily handled by using an appropriately curved fiber optic face plate set in oil against the plane surface of the input of the image intensifier described in the following section.

3.3 Image Intensifier

The requirement that the system resolve $\sim 1^{\circ}$ and the fact that the airglow features to be studied are known to move at $\sim 1^{\circ}/min$ at the zenith (Weber, et al., 1980) limited the exposure time to less than one minute.

This constraint, coupled with the expected brightness of the equatorial airglow (50 - 100R), mandated the use of an image intensifying device to get usable film densities. Two basic types of image intensifiers were considered for the camera system: A 25mm 3-stage so-called "first generation" image tube and a second generation microchannel plate (MCP) intensifier. Both tubes have similar gain, noise, and resolution specifications. However, the 25mm MCP intensifier (military specification: MX9644/UV) is one-third the length of the three stage tube, has an integral H.V. power supply (needing only

external 2.5V battery for power) and, most importantly, has antiblooming

characteristics that make it particularly well-suited for use in a situation

where a large dynamic range might be encountered(e.g., the moon's image

simultaneously with dim airglow). Figure 7 shows, in schematic form, the

operation of a second generation image intensifier.

Photons enter the fiber optic faceplate and strike the S20/25 photocathode

which is deposited on the inside surface of the faceplate. Photoelectrons

liberated at the cathode are then accelerated and electrostatically focussed

on the microchannel plate (MCP) electron amplifier. The MCP consists of a

parallel array of hollow glass cylinders about $10\,\mu m$ in diameter and about 1 mm,

or less, in length. The inside walls of the cylinders are coated with a secondary

emitting material. When a primary electron enters a cylinder, it cascades down

the channel producing additional secondary electrons.

Bonded to the output end of the MCP is a thin aluminum barrier and a

P1/P39 phosphor screen which converts the electron current back into photons.

Data sheets describing the characteristics of the intensifier used in the

all-sky system are included as an Appendix to this Chapter.

3.4 Camera

To photographically record the image from the output phosphor of the

intensifier, a transfer lens system and a standard 35mm single lens reflex

camera were used. A more efficient method of coupling this image to the film

would be to have the emulsion of the film pressed against the fiber optic

output of the image tube. This method permits all of the light from the phosphor

to enter the emulsion. However, a film transport mechanism to accomplish this

is a custom made device - and most importantly, if such a system is employed,

the image cannot be viewed in real time.

PHOSPHOR

FIBER OPTIC
FACE PLATE

MCP

BAFFLE

PHOTOCATHODE

FIBER OPTIC

FACE PLATE

VACUUM

$h\nu$

$h\nu$

e^-

e^-

$h\nu$

$h\nu$

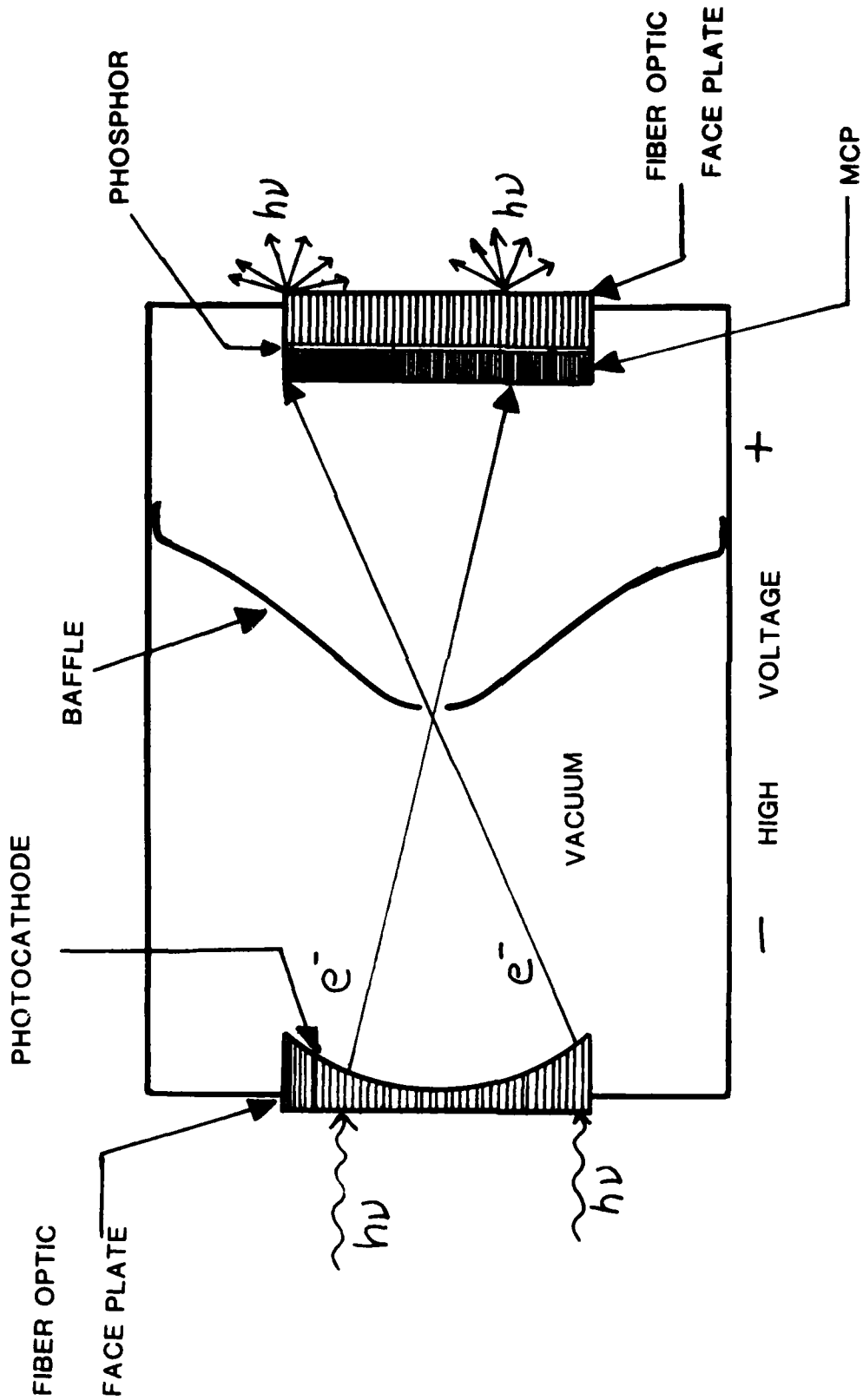$-$ $+$

HIGH   VOLTAGE

FIGURE 7

The penalty for optically transferring the output phosphor to the film is rather severe - only about 10% of the light from the intensifier can be coupled to the film emulsion with transfer lens systems operating near F/1. Special "fast" lenses have been designed to operate at conjugate ratios of 1:1 to address this demanding situation. However, it was found that commonly available "fast" lenses for 35mm cameras could be used in tandem pairs to produce as efficient transfer systems. In such a system the lenses are placed front to front so that the lenses are used at their designed infinite conjugate ratios. The first lens acts as a collimator while the second reimages the collimated beam on to the film. Such a system suffers from vignetting but with care this can be minimized. In the current system an 85mm F/1.8 Nikon lens is used as the collimator and a 55mm F/1.2 Nikon lens is used on the camera. This combination of focal lengths produces an image on the film 2/3 the size of the image on the output of the intensifier and keeps the total vignetting of the system to less than a factor of 3 over the image (see Figure 8). When used in the all-sky mode with the camera pointed at the zenith, this vignetting is partially offset by the Van Rijn brightening at large zenith distance. However, when the system is used with a narrow ($\approx 60^{o}$) field of view lens the vignetting is very noticeable.

A Nikon F camera body with a motor driven 250 exposure back is used to record the images. The camera back has been modified to allow data (time, date, etc.) to be recorded along one side of each exposure. The camera is operated by an external intervalometer built specifically for the Ascension Island campaign. The interval between exposures can be set to $2\frac{1}{2}$, 5 or 10 minutes and the exposure time can be varied by factors of 2 from 1/1000 sec
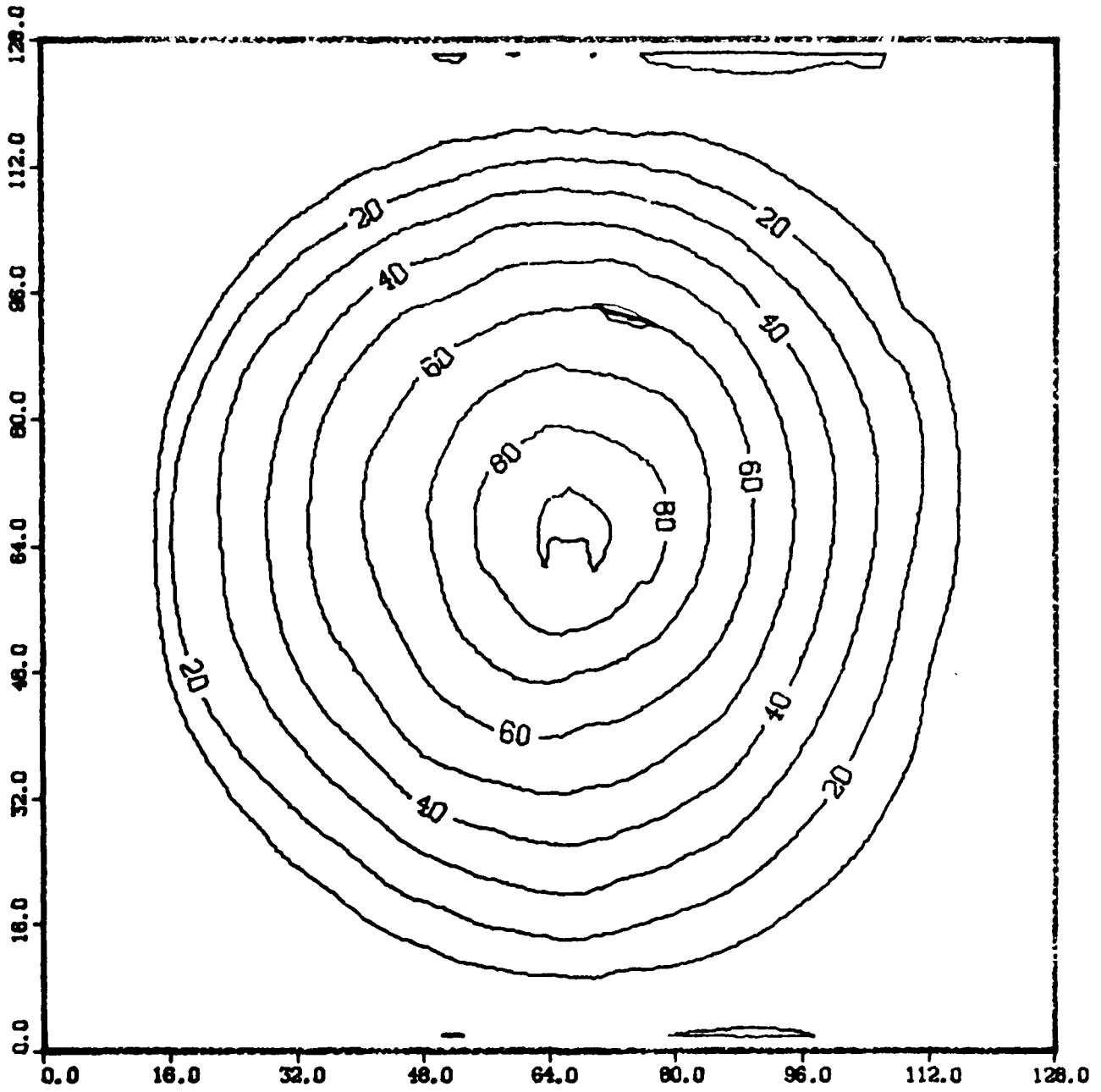
VIGNETTING FUNCTION

FIGURE 8

to 32 sec. A schematic of the completed system and the system set up in the field are shown in figures 9 and 10.

4. Measured Performance

4.1 Sensitivity

Sensitivity is defined here as the minimum exposure in Rayleigh-seconds (RSEC) to produce a density 0.3 above the combined density of the base of the film and fog and tube noise.

Several film were investigated until KODAK TRI-X developed in D-19 for 5 minutes was selected as best for overall speed, resolution, and availability. Using this film and the above definition the sensitivity of the system is 800-1000 RSEC.

4.2 Resolution

Field tests of the system have demonstrated that the system can resolve features smaller than 1° at the center of the field of view of the fisheye lens. This corresponds to about 12 lp/mm at the image plane of the system.

4.3 Real time viewing of weak airglow

At Ascension Island airglow depletions could clearly be seen in the viewfinder of the camera. A clear focusing screen and a 6x magnifying viewer were used to maximize the brightness of the image. An RCA ultracon T.V. camera "looking" into the camera viewfinder proved not to have the sensitivity to produce usable images.

4.4 Operation under high background conditions

During the Ascension Island campaign no adverse lighting conditions were encountered. The campaign was scheduled so that the moon was below the horizon during the hours of interest. However the narrow bandwidth of the filters used

INTENSIFIED CAMERA SYSTEM

60°LENS

180°LENS

24mm DIAMETER FIELD LENS
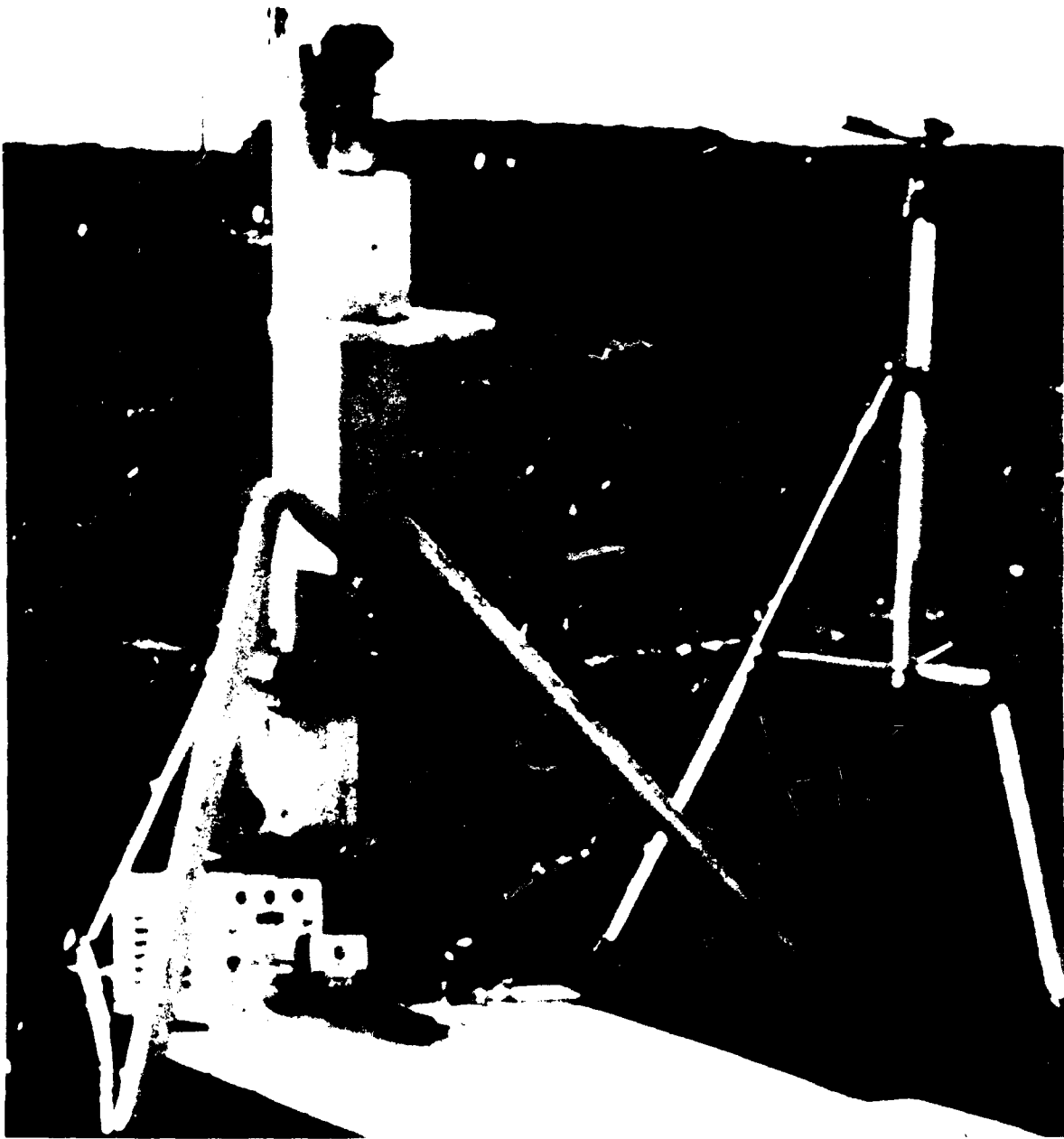
F/2.8 COLLIMATOR LENS

INTERFERENCE FILTER
(1 OF 4)

F/2.8 OBJECTIVE LENS

25mm 2nd GENERATION
IMAGE INTENSIFIER

F/1.2 COLLIMATOR AND
OBJECTIVE LENSES

FIGURE 9

35mm SLR CAMERA WITH
250 EXPOSURE BACK
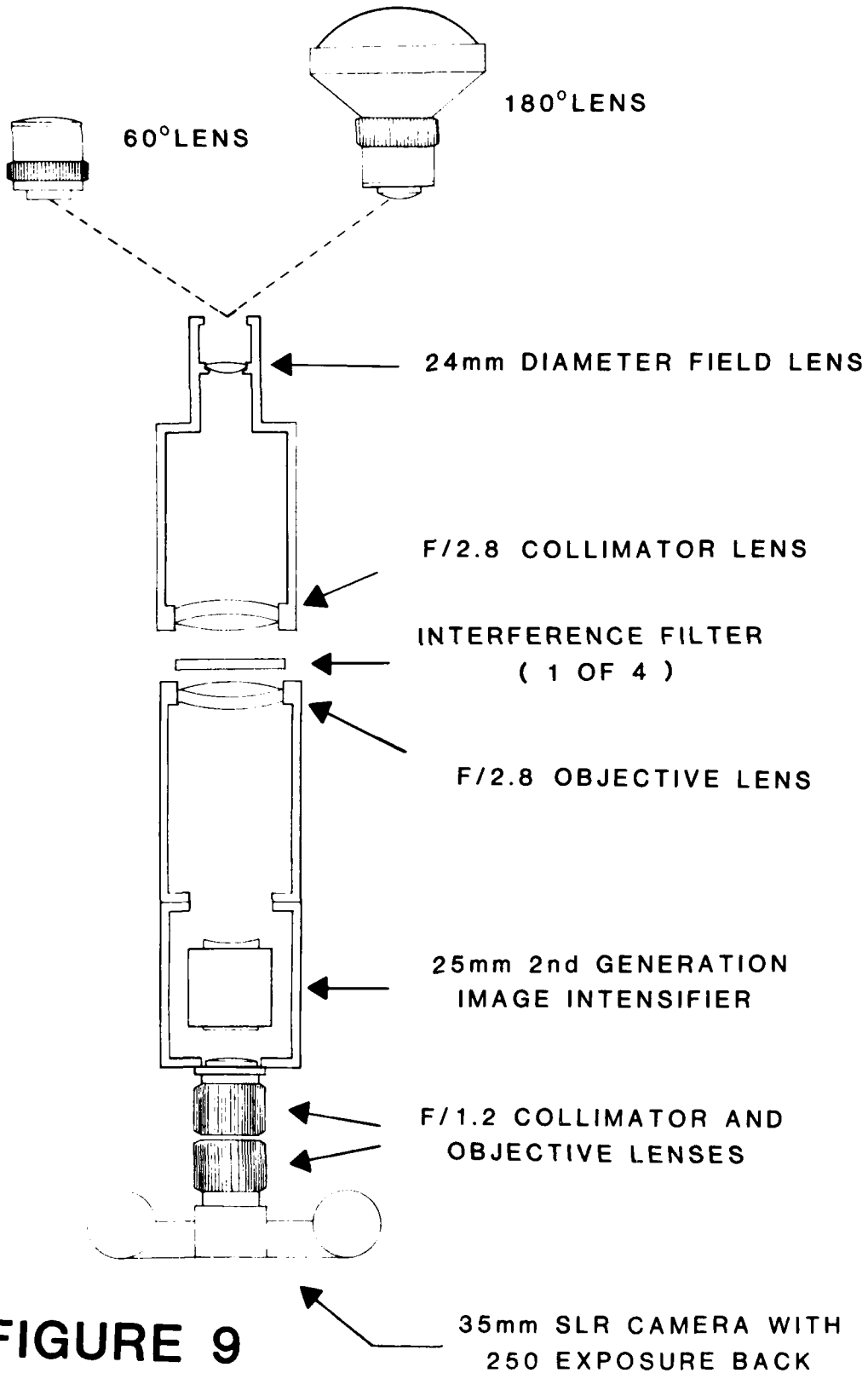
FIGURE 10

(12A) allowed useful airglow measurements to be taken starting at solar zenith angle ∿ 100°.

The system was used to monitor a rocket launch for Vandenberg AFB on June 23, 1981. (see Chapter 5), This was an "experiment of opportunity" and as such the launch data and time were dictated by the needs of the spacecraft orbit and not our desire to monitor the ionospheric effects of the launch vehicle. The 3rd quarter moon was 60° away from the airglow cloud and was imaged onto the photocathode of the image intensifier by the 180° fisheye lens. An example of a photograph taken during this event is hown in Figure 11. It can be seen that the moon's image did not prevent useful data from being taken.

4.5 Interchangeable lenses

For the June rocket campaign the system was configured with a 60° field of view objective lens. 5 minutes or so after the launch the airglow cloud exceeded this field and the 60° field lens was replaced by the fisheye -- a process that takes about 5 seconds. A series of photographs taken with the 60° field of view lens are shown in Chapter 5.

4.6 Photometric accuracy of the system

Chapter 3 discusses at length the photometric reduction techniques applied to the data taken with the intensified camera system.

5. Future Modifications

Some modifications planned to the intensified system include:

1. addition of different wavelength filters;

2. increasing the coupling efficiency between the output of the inten-
    sifier and the film;

3. the addition of a more sensitive TV camera to the view finder;

4. a more flexible intervalometer;

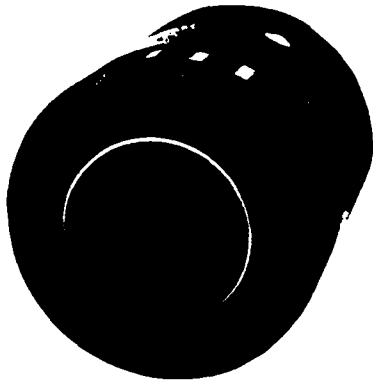5. addition of a thermostatically controlled oven for the filter wheel.

OPTICAL SIGNATURE OF AN IONOSPHERIC HOLE

ATLAS-F ROCKET LAUNCH -- 23 JUNE 1981

MOON

HORIZON

6300A AIRGLOW PHOTOGRAPH TAKEN

WITH ALL-SKY INTENSIFIED CAMERA

FIGURE 11

NVP

NIGHT VISION PRODUCTS

- · **Ruggedized construction**
- **Bright source protection**
- · **Lightweight**
- ı · **Short length**
- · **Low distortion**
- ·\ **High signal-to-noise ratio**
- **▪ Fast recovery time**

F 4727
IMAGE
INTENSIFIER
(MX-9644 UV

ITT Type F4727 25 millimeter microchannel electrostatic inverter is a single stage high gain image intensifier tube for use under low light or near infrared ambient conditions particularly in the scotopic regions of human vision (10^{-6} to 10^{-2} fc scene illumination)

The tube consists of an S-20/S-25 photocathode with extended red response deposited on a fiber optic input window a microchannel plate (MCP) electron amplifier and a green P-1/P-39 type screen fabricated on the fiber optic output window. The tube is completely self-contained with an integral power supply featuring manual gain control for low light levels and automatic brightness control (ABC) for uniform image output during exposure to high visible or near infrared radiation levels. The tube is also provided with bright source protection (BSP) circuitry to prevent damage to the tube in the presence of small bright light sources in the field of view. All high voltage is contained internally and the unit may be powered by a low-current 2.7 volt battery or other 2.4 to 3.2 Vdc source.

Performance environmental and physical characteristics of the ITT Type F4727 Image Intensifier are defined on the following pages of this data sheet

PERFORMANCE

PHOTOCATHODE

Entrance Window	Plano surface fiber optic
Photocathode Type	S-20/S-25
Useful Diameter	25mm

SCREEN

Exit Window	Plano surface fiber optic
Phosphor Type	P-1/P-39 Aluminized
Useful Diameter	25mm

MANUAL GAIN CONTROL WIRING DIAGRAM

The manual gain control operates in conjunction with a 50 thousand ohm gain control and a 470 thousand ohm resistor. The minimum manual gain setting is obtained with the wiper at position 1. The maximum manual gain setting is obtained with the wiper at position 3

+2 5 VDC Nominal
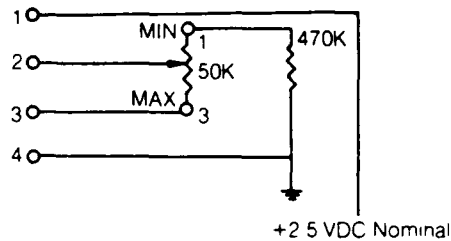
	MIN	TYPICAL	MAX	UNITS
Photocathode Luminous Sensitivity	200	350		µA/lm
Radiant Sensitivity				
@ 0 8 nanometers	12	30		mA/W
@ 0 85 nanometers	8	15		mA/W
Equivalent Background Input		1×10^{-11}	3×10^{-11}	lm/cm^2
Luminance Gain	20.000	50.000	70.000	
Center Resolution	25	30		line pairs/mm
Peripheral Resolution	25	30		line pairs/mm
Luminous Uniformity		1 5 1	3 0 1	
Magnification (over 25 mm dia)	96	1 01	1 04	
Distortion (over 25 mm dia)		4 0	5 0	%
Weight		310	350	grams
Useable Cathode Diameter	24 5	25		mm
Input Voltage	2 4	2 5	3 2	Vdc
Input Current		17	35	mA
Axial Eccentricity*		0 10	020	inch

* Alignment difference
of optical and mechanical
centers at output of tube

ENVIRONMENTAL

Temperature Range (Storage)	-62°C to +68°C
Temperature Range (Operating)	-54°C to +52°C
Vibration	10 to 3500 Hertz at 2 5 g peak sine wave
Shock	500 g for a 3 milli-second duration
	140 g for a 9 milli-second duration
Operating Position	Any
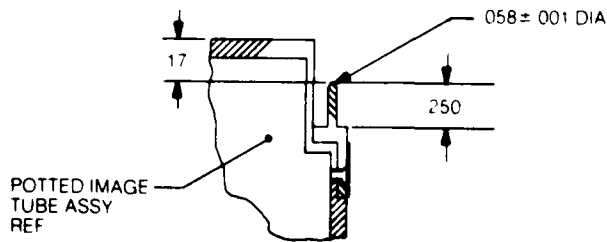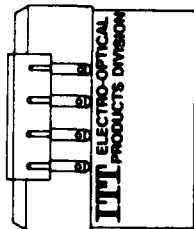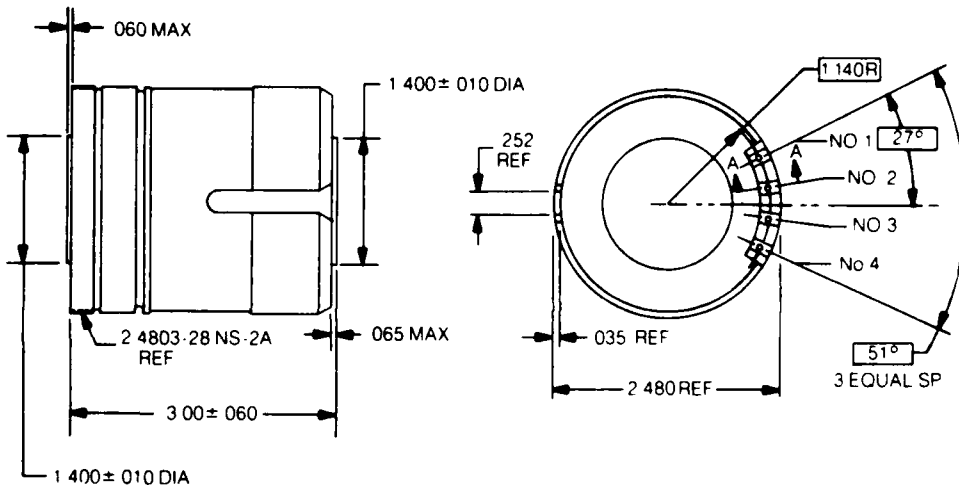
PIN	CONNECTIONS
1	+2 7 VOLTS
2	GAIN
3	GAIN
4	GROUND

TYPICAL GAIN SATURATION CURVE
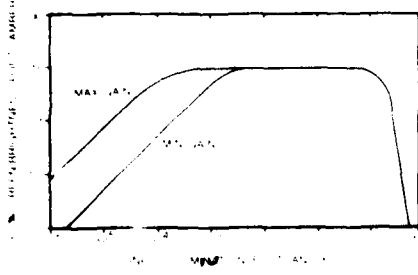
TYPICAL MODULATION TRANSFER FUNCTION
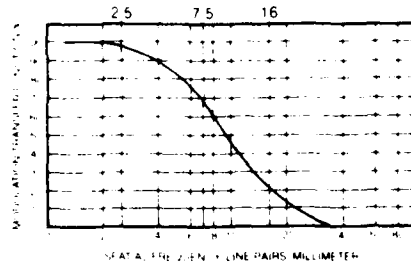
SPECTRAL OUTPUT P-1 P-35 PHOSPHOR
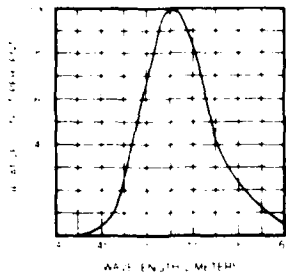
TYPICAL ABSOLUTE SPECTRAL RESPONSE CHARACTERISTICS OF VARIOUS PHOTOCATHODES ON FIBER OPTICS

9/78

ITT ELECTRO-OPTICAL PRODUCTS DIVISION ITT
7635 Plantation Rd., Roanoke, Va. 24019. Telephone (703) 563-0371

25MM IMAGE INTENSIFIER ASSEMBLY F4727
MICROCHANNEL INVERTER

SERIAL NO. _9061_

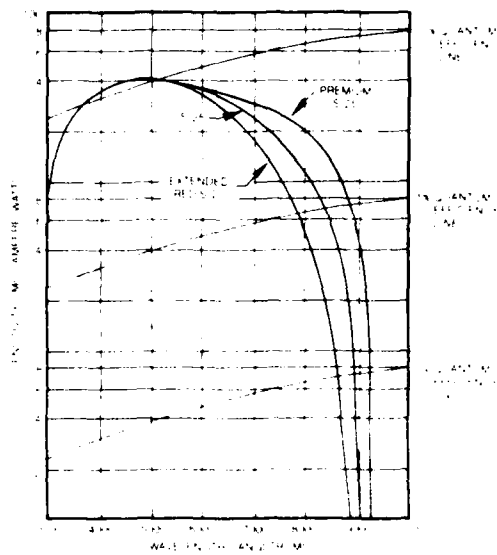| TEST	MIN.	ACTUAL	MAX.	UNITS
PHOTORESPONSE				
2854°K	200	334		µA/lm
8000 A	12	27.0		mA/W
8500 A	8	12.0		mA/W
CYCLIC OPERATION		OK		
EBI		.52×10⁻¹¹	3 × 10	lm/cm
LUMINANCE GAIN	20,000	57,193	70,000	
CATHODE & SCREEN QUALITY		OK		
FPN				
MULTI MULTI	-15	OK	+15	%
MULTI-BOUNDARY	-20	OK	+13	%
CENTER RESOLUTION	25	32.0		lp/mm
MECHANICAL INSPECTION	(RT-212,071 and RT-201,264)			

1. - SCREEN/RETAINER _✓_
2. - CATHODE HEIGHT _✓_
3. - ASSY. HEIGHT _✓_
4. - HOUSING EXT. THREADS _✓_
5. - MARKING _✓_

6. - COMPONENTS/MATERIALS _✓_
7. - WORKMANSHIP _✓_
8. - PIN SPACING _✓_
9. - CATH. FLATNESS _✓_
10. - SCREEN FLATNESS _✓_

TESTED BY: _L. CLARK_
REVIEWED BY: _B. Perdue_

DATE SHIPPED: _2-22-81_
S/O NO. : _RA-81046_

MANUAL GAIN CONTROL WIRING DIAGRAM

The manual gain control operates in conjuction with a 50 thousand ohm gain control and a 470 thousand ohm resistor . The minimum manual gain setting is obtained with the wiper at position 1. The maximum manual gain setting is obtained with the wiper at position 3.

1
2
3
4

MIN 1
50K
MAX 3
470K
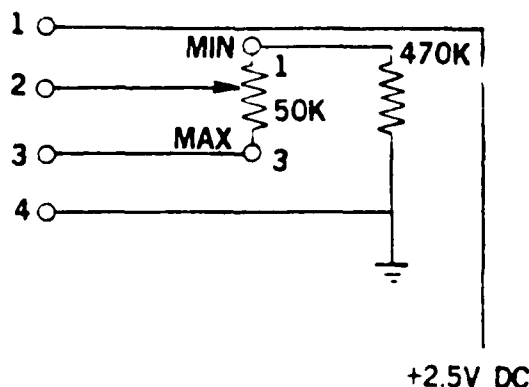
+2.5V DC

CHAPTER 3

DATA REDUCTION AND IMAGE PROCESSING

1. Introduction

In this chapter, a discussion of the various types of data reduction and analysis will be given for the data gathered during the Atlas-F rocket launch of June 1981, and the Ascension Island equatorial airglow depletion campaign of January 1981. The nature of the data reduction concerned the processing of data captured on 35 mm film to some form of visual display capable of relating qualitative, as well as quantitative information. Initially, prints were made of the frames describing the events and simple overlays were created to characterize the gross features. Later, these same data were digitized, and through a library of computer programs, were produced graphically in a manner more conducive to scientific investigation.

The first method of analysis for the airglow images was developed for the Ascension Island data. A series of three computer generated overlays were developed for use on the photographic prints of the airglow depletions. The first overlay, created from a starfield taken at a known time, was used to determine the altitude and azimuth of any given point in the field-of-view. The second overlay, computed for a specific airglow height, could be used to determine the subionospheric geographic coordinates of a depletion. Finally, the last overlay produced a set of magnetic meridians, again, at a given height above the Earth. These overlays could be used to give quantitative information, such as airglow depletion drifts, spatial extents, and alignments with respect to geomagnetic coordinates. In addition, for the rocket data gathered, one similar type of overlay was devised. This overlay displayed the trajectory of

the Atlas-F rocket, projected onto an altitude-azimuth grid with times-of-flight and corresponding rocket heights.

2. Digital Analysis Methods

Digitization of the data by the Eikonixscan system yielded 512 x 512 arrays of 8 bit transmission numbers. It was decided to reduce the size of these large arrays for several reasons. Primarily, the resolution of the all-sky monitoring system with the fish eye lens (180 degrees) ranged from 1.0 to 2.0 degrees, and about three times greater with the narrow field lens (60 degrees). Thus, an array 512 x 512 in size would oversample each frame, in effect creating detail that was beyond the optical limit of resolution. In addition, the reduction of the array served to smooth out any anomalous pixel to pixel discrepancies and/or scratches or emulsion defects (e.g., pinholes, dust, etc.) on the film itself. Finally, from a practical stand-point a smaller array was much faster to process in digital computations.

In order to reduce the array size, and still maximize the three criterion mentioned above, i.e., (1) to approach a size comparable to the resolution without creating or destroying detail, (2) to smooth our troublesome pixel noise without suppressing meaningful data, and (3) to choose the smallest possible array to promote speed and efficiency in processing, it was decided to use a 128 x 128 pixel array. This size was obtained by a simple averaging of adjacent 4 x 4 regions to create the final 128 x 128 format used in all following discussions.

In addition to the data taken in the field, control data were also digitized so that a means to go from transmission units to intensity units could be established. Using the same all-sky camera set-up, a standardized light source

was photographed across its range of graduated intensities using different exposure times in order to simulate the conditions under which the field data were gathered. After digitization of these uniformly illuminated frames, both with and without a 1.0 neutral density filter, the center 5 x 5 pixel region of each array was averaged (to avoid possible vignetting effects). The end product of such a procedure was a transmission-to-intensity look-up table for different exposure times and filter combinations. To find the intensity corresponding to a given transmission number, it was necessary to account for whether the frame was digitized with or without a filter, and what the corresponding exposure time was; the table then yielded the correct intensity value.

Before the intensity transformation could be carried out, it was necessary to correct for any non-uniformities present in the digitizing system. This was accomplished by digitizing a field with no negative in the film carrier. This so-called "flat-field" array, in the absence of non-uniformities of illumination and diode sensitivities, should have the same value everywhere. The transmission numbers in the actual "flat-field" array showed about 15% variation over the field digitized. By normalizing this flat field frame to the highest transmission value, an array was obtained, which when divided into any other data array in transmission units, would correct for unevenness of illumination of the negative being digitized.

In addition to the "flat-field" correction, it was clear from the design of the all-sky imaging system that internal effects, such as the vignetting encountered in reimaging the output phosphor of the intensifier, as well as external factors, such as the van Rhijn effect, must be addressed. Due to experimental circumstances, these problems were approached in different ways

in regards to the Atlas-F rocket launch and to the Ascension Island depletion campaign. First, the rocket launch data analysis for vignetting correction is discussed.

To produce a vignetting array, a frame was digitized that contained a uniform signal, i.e., a frame which was exposed while the camera system was monitoring an evenly illuminated diffuse source. While the array was in transmission units, the standard "flat-field" correction was applied, and, as described before, the appropriate transformation to intensity was performed. Again, as with the "flat-field" array, this the so-called "vignetting" array, was normalized to its highest value. Similarly, it was then used to correct other data arrays after they were transformed to intensity units.

Before this correction was actually applied, it became apparent that the vignetting array was a bit noisy, though it did resemble closely the characteristic bulls-eye pattern of an analytically defined vignetting function. After repeated attempts at two-dimensional spline fits it was decided to use a simple 5 x 5 running average scheme. This type of averaging involved moving one pixel at a time and averaging the surrounding 25 pixels. This method was by far the most successful at smoothing large spikes, while at the same time, it was equally effective in maintaining detail and a close resemblance to the raw unsmoothed data. Thus, this method resulted in creating a workable vignetting array which was an essential tool for contouring routines.

For the Ascension Island airglow depletion photographs, different physical conditions led to a revised analysis of vignetting and van Rhijn effects. In contrast to the rocket data, the Ascension Island data were taken only with the 180 degree fish-eye lens. A new approach was taken to correct for vignetting and van Rhijn effects together.

Inspection of all the photographs digitized showed that no one area of the sky was preferred by depletion activity. After choosing two representative days, (Feb. 1 and 2, 1981), each frame was corrected for "flat-field" and put into intensity units. Then, all the image arrays for a night were averaged together and, finally, the two night's averages were combined in a grand average, the so-called "average frame." This average frame was then smoothed by the 5 x 5 pixel averaging method described above. The end result was an "average frame" that yielded the combined mean total of the vignetting of the system, the van Rhijn effect of the atmosphere, the background intensity of the airglow, and the stationary objects which were unwanted, such as telephone wires (see figure 1).

The average frame was used in two separate ways. In the first technique the average frame was subtracted from the data array to form a "difference image." In such a format, all stationary objects and constant airglow features went to zero, and if a constant factor was added to the array, the depletions appeared as indentations along a continuum. While this method did not really address the issues of vignetting and the van Rhijn effects, nor was it capable of producing absolute intensities, it was quite effective when used to display the essential characteristics of airglow depletions as departures from mean conditions.

The second technique took the average frame, normalized it to the peak value in the array, and divided it into each of the data arrays. This resulted in a good correction for the combined effects of vignetting, van Rhijn, and local time difference from east to west, but did not totally "erase" the presence of the stationary objects in the field-of-view. This method was essential for determining the true slopes of the walls of the depletions and was the

preferred correcting function to apply for contouring purposes.

In summary, for both the Atlas-F and the Ascension Island projects, the data reduction followed along quite similar lines (see figure 2). Each photograph was digitized to a 512 x 512 pixel array that reduced subsequently to a 128 x 128 array by a straight 4 x 4 averaging in transmission units. These arrays were then corrected for flat-field, converted to intensities via an appropriate look-up table, and then corrected for the corresponding vignetting and van Rhijn function. By inspection of control filters at 6200$\overset{o}{A}$ for both events, it was decided that any background light, aside from the 6300$\overset{o}{A}$ airglow, was below the sensitivity of the system and could therefore be ignored in the reductions. The final data arrays were usually still somewhat noisy to be of practical use in further computations. Thus, in nearly all cases, a 5 x 5 running average technique was applied to help smooth the data for final analysis or display.

3. Graphical Display of the Final Data Arrays

The ionospheric hole created by the rocket was the first data to be graphed and had a few problems associated with it. The airglow burst recorded was on the order of 14 kilorayleighs, far above an almost negligible background. In order to increase the effective dynamic range of the scanning system, these frames were digitized both with and without a filter. This was done in the hope that a linear relation could be found between the two resulting arrays. However, due probably to scattered light in the digitizing system, no such relation was clearly defined. This resulted in the high end of the intensity scale (i.e., the densest part of the negative) to exhibit a fair amount of

uncertainty.

Since a calibrated photometer was used in conjunction with the imaging data taken during the rocket experiment, absolute values of intensities could be fixed to the data. Simply by knowing where the photometer was pointing, the corresponding pixel in the array could be monitored over time and essentially matched to the photometer tracing along the same interval to produce a means of calibration to absolute intensity. These intensities were then transformed to log (intensities) due to the wide range of values encountered during the event.

In graphing these data, it became necessary to suppress extraneous signals from the intensifier that were beyond the edge of the actual field-of-view of the camera. The first contouring method involved drawing isophotes at certain prescribed levels on a two-dimensional graph ('x' pixel vs. 'y' pixel). This type of plot showed well the way in which the hole progressed in both shape and size over time. Specifically, for example, a certain intensity level could be watched to estimate expansion rates. The other type of contour graph consisted of taking this two-dimensional grid, projecting it in the "z" direction, and then dropping a net or fine mesh atop it. In this way, a three-dimensional representation of the phenomenon could be presented, where the hole appeared as a hill above the background airglow. The best feature of this technique was that the graph could be rotated to allow various viewing angles so that details in the structure of the hole, i.e., the observed "horshoe pattern", could be followed as it changed over time. Plots of all the digitized 60 degree frames are given in Figure 3.

Many of the digital display schemes developed for the rocket launch effects were subsequently used for the display of the airglow depletions recorded at

Ascension Island. Because the range of intensities of the depletions were much less, no filter was needed in digitizing and thus confidence in intensity values were good. However, without the benefit of photometer readings, the best that could be arrived at were relative intensity levels. For the most part, as mentioned before, the use of log (intensities) was not required as the range of values was not as large as the rocket event.

As with the rocket data, both types of contouring routines were used for the equatorial depletion data. Again, the signals exterior to the actual field-of-view were suppressed and viewing angles, where necessary, could be altered to sight down depletion "valleys." In the end, each type of presentation was useful to show the finer structures of the features and to show the temporal progression of the depletions.

In addition to these contour plots, a third type of graph was developed for the Ascension Island data. Before performing the 5 x 5 running average on the corrected arrays, the line of numbers running from the east horizon to the west horizon through the zenith, the so-called "prime vertical" was extracted. Using the fact that Ascension Island is close to the equator and that there existed a linear relation between pixel number and an arc-distance from the zenith, it was possible to convert pixel number to distance at any given height above the Earth. These prime vertical plots (relative intensity vs. distance) then could be used to calculate drift velocities as well as the slopes of the depletion walls.
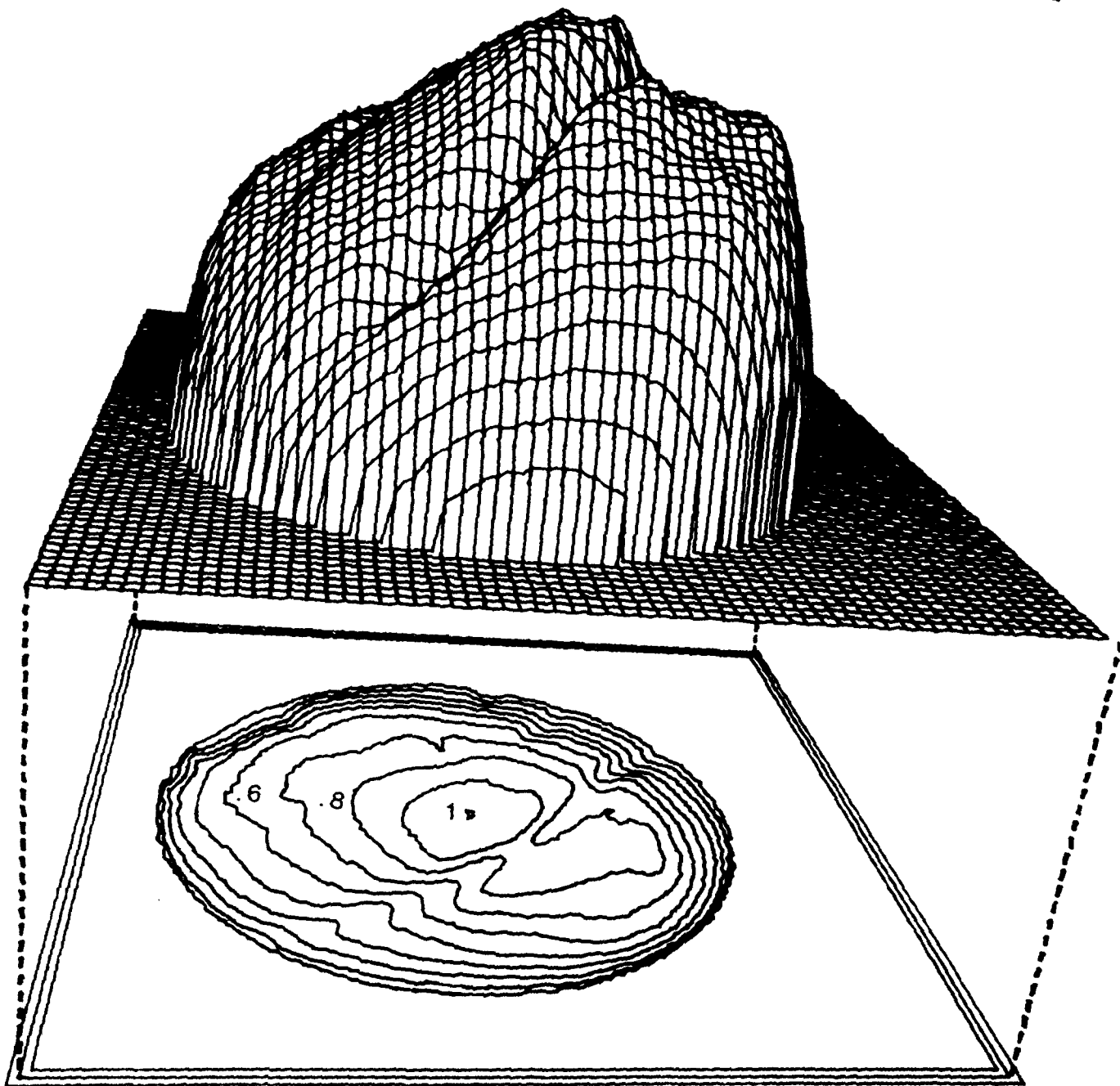
AVERAGE FRAME: FEB1 & FEB2
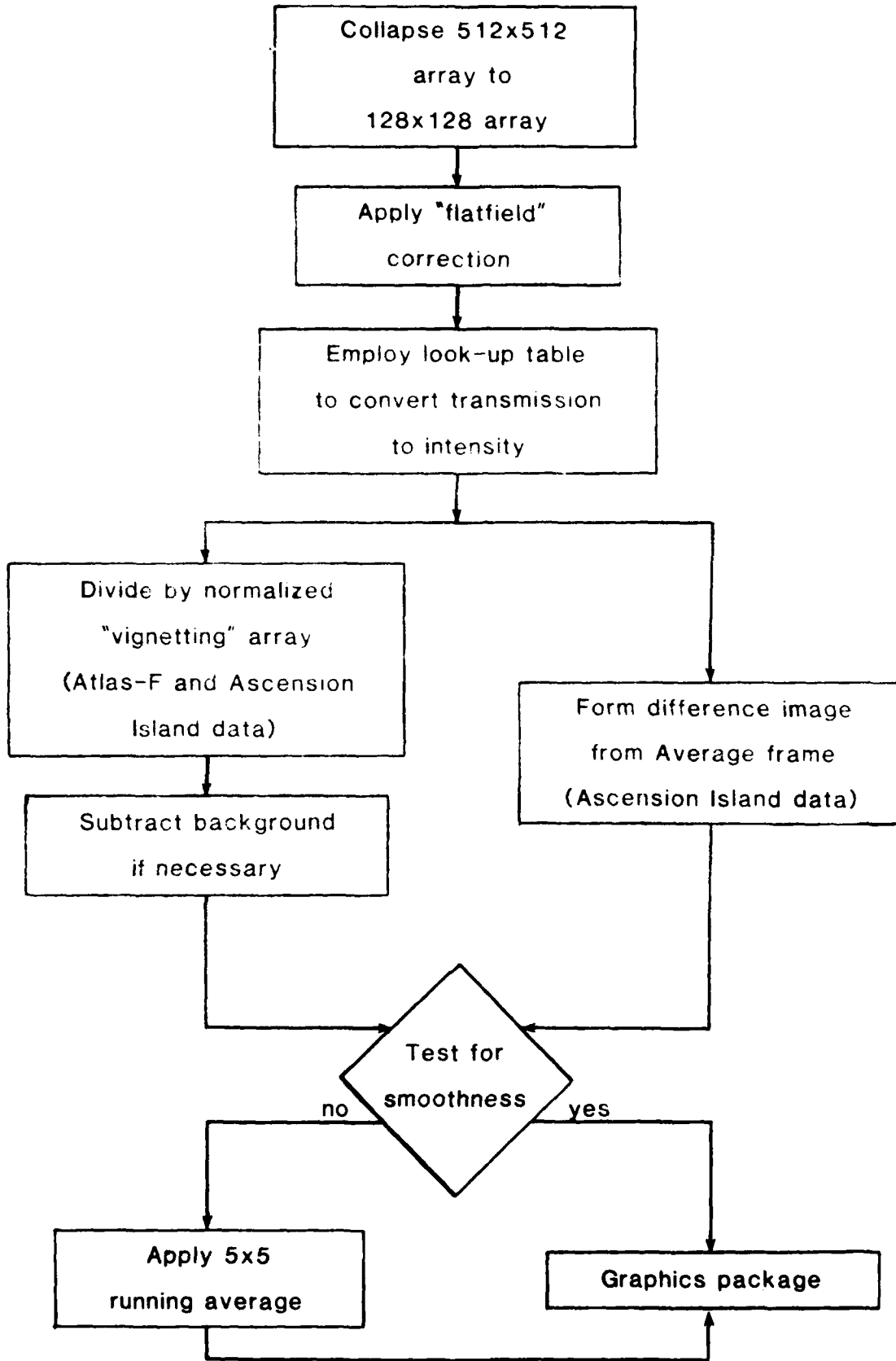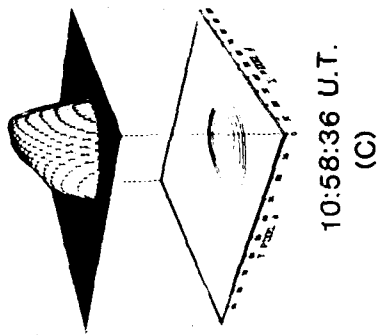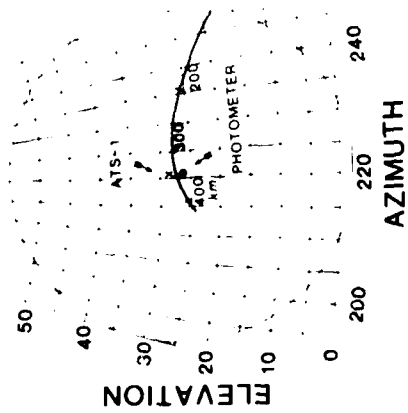

FIGURE 1:
Ascenion Island "vignetting" function.

FIGURE 2. Imaging Processing Technique
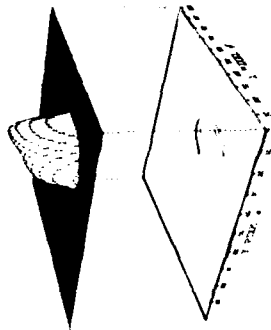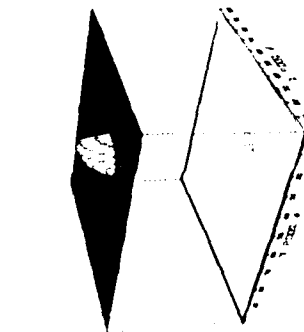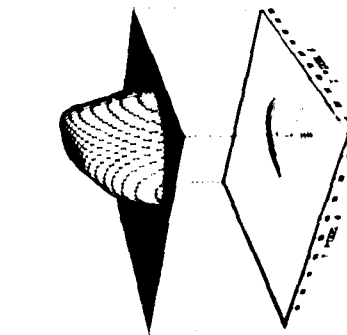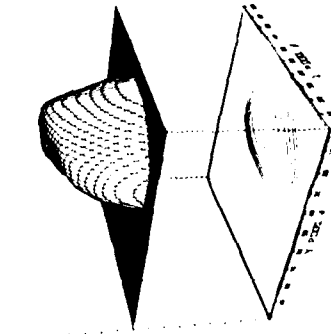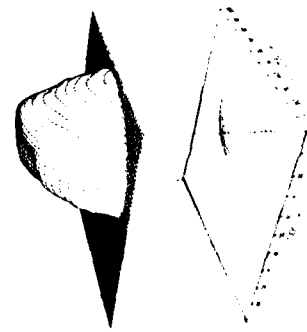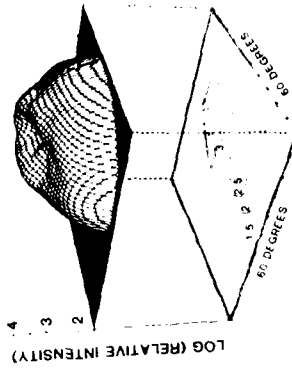
FIGURE 3. Digital image processing of airglow photographs

CHAPTER 4

AIRGLOW CHARACTERISTICS OF EQUATORIAL
PLASMA DEPLETIONS

I. INTRODUCTION

Airglow observations have long been used to study the structure and
dynamics of the upper atmosphere (Cabannes, 1935; Bates, 1946). The oxygen
"red line" emission at 6300 $\overset{o}{A}$ offers a particularly convenient way of
monitoring processes in the lower portions of the ionospheric F-region
(Chamberlain, 1961; Peterson et al., 1966). Hays et al., (1978) have pro-
vided a recent description of the various sources and sinks of 6300 $\overset{c}{A}$
radiation in the ionosphere. During the nighttime hours, photochemical
equilibrium exists between the production of $O(^1D)$ atoms via the F-region
loss process

$$O^+ + O_2 \overset{\gamma}{\to} O_2^+ + O \qquad (1)$$

$$O_2^+ + e^- \overset{\alpha}{\to} kO(^1D) + (2-k)O \qquad (2)$$

and the decay of $O(^1D)$ by emission and quenching. The charge transfer re-
action (γ), the dissociative recombination rate (α), and the efficiency
factor (k) for the number of $O(^1D)$ states created per plasma recombination
are considered to be well-known parameters (Hays et al., 1978), and thus
the overall emission at 6300 $\overset{o}{A}$ depends on the height profiles of O_2 and e^-.
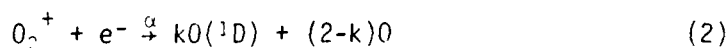Since the equatorial ionosphere exhibits a well-known "anomalous pattern"
for the height (hmax) and magnitude (Nmax) of its peak density, while the
neutral O_2 profiles are relatively uniform within $\pm$ 15° dip latitude of the
magnetic equator, the airglow emission at 6300 $\overset{o}{A}$ depends almost exclusively
upon the instantaneous structure of the $N_e(h)$ profiles. The morphology of

the F-region's equatorial anomaly has been reviewed recently by Anderson

(1981) and Anderson and Roble (1981); their results show that during pre-

midnight hours, the crests of the equatorial anomaly have h_{max} values

near 300 km, while at the equator h_{max} approaches 600km. This extra-

ordinary height variation accounts for the prominent intertropical arcs

or bands of 6300 Å airglow associated with the anomaly, as first discussed

in detail by Babier et al. (1961).

In recent years, airglow studies of the equatorial ionosphere have

concentrated on the departures from uniform airglow contained within the

broad intertropical arcs. This new approach resulted, in part, from a

new observing technique developed by Mende and Eather (1976) and Mende

et al. (1977) in which a TV system operating in an integrating mode, with

a wide field of view and a narrow spectral bandwidth, records monochromatic

all-sky observation of auroral and airglow emissions. Using this type of

instrument installed in the Air Force Geophysics Laboratory's Airborne

Ionospheric Obeservatory, Weber et al. (1978, 1980) obtained a remarkable

series of "equatorial airglow depletions" from all-sky imaging observations

at 6300 Å. The regions of decreased 6300 Å intensity were north-south

aligned, had east-west dimensions of 50-200 km, often extended to more than

1200 km in the north-south direction, and indeed were viewed as continuous

irregularity features spanning the magnetic equator to both intertropical

arcs. The depletions appeared after sunset and were observed to drift to

the east with speeds of 50-150 m/sec.

The 6300 Å airglow imaging technique pioneered by Weber et al, (1978,1980),

and recently extended by Moore and Weber (1981) to include images at 7774 Å,

has shown that the equatorial airglow depletions are linked unmistakably to

the equatorial F-region bubbles and plumes of plasma irregularities that have been the subject of intense study during the past several years (Matsushita et al., 1981). Radio and rocket-borne diagnostics of equatorial plasma depletions offer very detailed "line of sight" aspects of the phenomenon; all-sky optical methods offer broad, instantaneous coverage of the features, but only from the limited altitude range where natural airglow occurs. All three methods (radio, in-situ and optical) are clearly complementary. The imaging technique is still in its early phase, and promises to be a valuable method for quantitative, upper atmospheric science.

In this paper we wish to describe a new series of optical measurements obtained from ground-based, photographic methods. The results suggest that a substantial data base of equatorial depletion characteristics can be obtained during a relatively brief experimental campaign, and that the airglow images can be processed to yield quantitative descriptions of a broad range of parameters related to the theory and practical consequences of equatorial plasma irregularities.

In the following Section, our all-sky airglow imaging system is described. In Section 3, we describe a field test of the apparatus during an equatorial observing campaign in January - February 1981. Observations and results are discussed in Section 4, and a summary of findings appears in Section 5.

2. A LOW-LIGHT-LEVEL AIRGLOW
IMAGING SYSTEM

In equatorial regions the normal background of 6300 $\overset{o}{A}$ radiation is
relatively weak (~50-100 R). In order to detect regions of depleted airglow
in relatively short integration times (<1 minute), an intensified camera
system is required. The optical system developed for this purpose is shown
in schematic form in Figure 1. While the system has interchangeable all-sky
(180° field of view) and narrow (60° field of view) lenses, all of the observa-
tions reported on here were taken using the 180° field of view option. In this
mode, a standard NIKKOR 8 mm f/2.8 "fisheye" lens produces a circular image of
the sky 23 mm in diameter. The light from this image is collimated by a 100 mm
diameter f/2.8 lens before passing through a 6300 $\overset{o}{A}$ interference filter to reject
unwanted background radiation from the Moon and stars. The system was designed
for a filter having a very narrow bandwidth (6 $\overset{o}{A}$ FWHP); in the observations
reported here, an alternate 12 $\overset{o}{A}$-wide filter was used.

After passing through the filter, the monochromatic light is re-imaged on
the photocathode of a second generation image intensifier whose luminous gain
is approximately 60,000. The output phosphor is then imaged on 35 mm film
using two NIKKOR lenses front-to-front and a NIKON-F2 camera body. All of the
images discussed in this paper were taken at 10 minute intervals using a
30-second time exposure.

3. THE ASCENSION ISLAND EQUATORIAL

IONOSPHERE OBSERVING CAMPAIGN OF 1981

The Air Force Geophysics Laboratory organized a multi-techinque observing

program on Ascension Island (7.95 S, 14.38 W) during the period 24 January

to 10 February 1981. Boston University's all-sky airglow imaging

system operated from 27 January to 8 February and obtained useable airglow

data from 11 of the 13 nights. Figure 2 shows the location of Ascension

Island with respect to geographic and geomagnetic coordinates. It can be

seen that Ascension Island sits close to the southern crest of the equatorial

anomaly, essentially beneath the southern intertropical arc. The two circles

indicate the coverage of the camera system for zenith distances of 75° and

90°, respectively. In Figure 3, a sample photograph is shown together with

three types of overlay-grids used to examine the image features. Note that

the field of view for this and all subsequent photographs exhibits the usual

inversion of east-west coordinates. The field of view also contains a group

of four telephone-pole-size antenna poles, with connecting wires. These poles

are reproduced on the grids, and serve as convenient orientation markers, as do

the two building lights on the eastern horizon. The widths of the wires

illustrate the resolution achieved by the system ($1\frac{1}{2}^{\circ}$).

The grids presented in Figure 3 contain important information on the

spatial extent and characteristics of the images. Note that the zenith angle

grid (lower right) describes a nearly linear relationship between zenith angle and image size. The geographical grid above it shows that a zenith angle of 75 encompasses approximately ±8 of latitude/longitude from the zenith, which is equivalent to a horizontal diameter of ±1800 km through the zenith at 300 km. Between zenith angles of 75 to 90, an additional ±8 of latitude/longitude are encompassed, but compression effects render this region difficult to work with in any quantitative way. It is important to note, however, that the geomagnetic equator falls within the 75 - 90 region of the field of view, as illustrated in the lower left grid.

As a further aid to interpreting the photographs, Figure 4 gives a schematic representation of the airglow viewing geometry computed for the magnetic meridian of Ascension Island. The broad band near a height of 300 km depicts the approximate region of 6300 Å emission recorded by the optical system. From north-to-south horizon, this region spans 3600km, and shows that the airglow features recorded describe characteristics at the base of many field lines. Thus, at a zenith angle of ±85 to the south, the images recorded from airglow characteristics near 300 km pertain to field lines that cross the magnetic equator near 1850 km. Images recorded near the zenith pertain to flux tubes crossing the equator near 700 km, while images recorded at zenith angles ±85° to the north arise from 300 km features at the magnetic equator itself. Images taken from such a geometry have the interesting quality that features seen from top-to-bottom on the photographs have a one-to-one correspondence to altitude, bottom-to-top (≃300 km to ≃1800 km), above the equator. When interpreted in this way, the optical imaging technique can be seen to yield information about the height-dependence of plasma depletions above the equator, as well as the broad morphology aspects inherent in an all-sky photograph.

IV   RESULTS

Figure 5 contains a summary of a night's observations from Ascension

Island. Located close to 15°W, local time at Ascension is approximately 1

hour earlier than the U.T. values shown in the figure. The bright image

of the setting moon is seen in the upper right corner of the frames at 21:00

and 21:10 U.T., and the bright dot near the two building lights in the lower

left results from the combined images of Jupiter and Saturn. The availability

of useable airglow data for depletion related studies, as shown here for

7-8 February 1981, is typical for that obtained on other nights. The back-

ground airglow usually increased after 21:00 U.T., generally revealing well-

formed depletions. After 01:00 U.T., the depletions gradually disappeared

and observations were ended for the night.

Figure 5 exhibits a rich display of equatorial airglow depletion shapes

and forms. Frame 22:20 U.T. alone shows narrow bands, twisted features, air-

glow islands and a "wishbone" formation. Later in the evening, single large

depletions dominate the scene. Figure 6 gives further examples of narrow depletion

bands (1 Feb'81, top panels) and a second "wishbone" feature (2 Feb'81, bottom

panels). Figures 5 and 6 illustrate several morphology features that can be

characterized using simple overlay/grid data reduction techniques. These

include depletion occurrence rates, alignment characteristics and large-scale

drift speeds. More detailed image processing methods applied to special features

(such as the "wishbone") and to individual depletion edge effects will be described in a following section.

4.1. Depletion Occurrence Rates and Spatial Coverage

During the 13-night optical observing program on Ascension Island, two nights were completely cloudy and no 6300 A emission was observed. On three of the remaining eleven nights, there was a bright 6300 A airglow, but no depleted regions were observed. Thus, on eight of the eleven clear nights (~70%), well-formed airglow depletions were photographed throughout the evening hours.

As noted in the previous section, regions of depleted airglow usually appeared after 20:00 L.T., disappear after midnight, and occurred most abundantly during the 20:30-23:30 L.T. hours. Baumgardner and Klobuchar (1981) analyzed each photograph containing depletions with an equal-sky-area grid in order to estimate the portion of the sky covered by depletions. To avoid compression effects near the edge of each photograph they limited their analysis to zenith angles down to 70°. Their results, summarized in Figure 7, show that on several nights the depleted regions covered over 30% of the sky for extended periods, and on a few occasions over 40% of the sky. Averaging over the samples available, one concludes that on nights when depletions occur, approximately one-fourth of the sky is covered by depletions for at least two hours.

4.2. Depletion Alignments

In the first study of wide-angle imaging of equatorial airglow depletions, Weber et al., (1978) described the depletions as "north-south" aligned. Their observations were made along a magnetic meridian near Lima, Peru, from an aircraft that kept within $\pm 3^\circ$ of the magnetic equator. They noted that the depletions were basically aligned with the magnetic meridians close to the equator, but that a skewness was evident for depletion ends extending far from the equator. In their subsequent study (Weber et al., 1980), the aircraft flew in

a region above and to the north of Ascension Island, and recorded several cases of the poleward ends of depletions curving noticeably to the west. As described in Figure 4, ground-based photographs from Ascension Island are particularly useful for documenting alignments since the magnetic equator appears near the very top of the photographs. Horizon-to-horizon depletions in the N-S direction thus extend over 3000 km from the equator, and departures from magnetic meridians can be seen to grow from top-to-bottom. For example, consider the depletion shown in Figure 3. The central depletion begins due north on the magnetic equator. The grid below it shows that if the depletion were aligned along a magnetic meridian, it would curve to the left in the photograph. Instead, as one progresses down the axis of the depletion, it appears on meridians 2°, then 4°, and at the bottom, up to 8°-10° to the west. Since features at the bottom of the photograph relate to altitudes far above the equator, this westward tilt must be the optical manifestation of the westward tilts of plasma depletion plumes recorded by incoherent scatter radar (Woodman and La Hoz, 1976; Tsunoda, 1980) and by in-situ probes (McClure et al,. 1977). The end result of these strong westward tilts is that from a site such as Ascension Island, where the magnetic declination is large ($\approx 20^\circ$) and to the west, the depletions appear to be geographically-aligned in the North-South direction. This is, of course, an artifact of the geometry, and not a physically important characteristic.

4.3. Large-Scale Plasma Drifts

Weber et al., (1978) described several cases of airglow depletions that were observed to drift eastward, with speeds of 50-100 m/sec., for up to several hours. Figures 5 and 6 show that eastward drifts are clearly visible in 10-minute spaced photographs from Ascension Island. Using the eight nights of airglow images that contained depletions, we computed eastward drift speeds for optical features crossing the zenith as a function of local time. Using photographs taken 10

minutes before, on , and after the hour, drifts were computed for features

(dark or bright) close to the zenith, using an assumed height of 300 km. In

some cases, when a photograph was rich in detail, two sets of speeds were

computed for a given hour. The results of this analysis are given in Figure

8, where the average speeds (with numbers of observations in parentheses) are

plotted as a function of local time. Figure 8 also contains several sources

of comparison with measurements made by other techniques:

(1) The Sipler and Biondi (1978) results refer to the average thermospheric

wind detected by the Fabry-Perot interferometer method, from five days of

observations at Kwajalein, during August-September 1977. The Sipler et al.

(1980) results refer to similar measurements during five days in July 1979.

(2) The Aarons and Whitney (1980) results were obtained by analyzing spaced

receiver scintillation records from 13 nights in March 1977 at Ancon, Peru.

(3) The Fejer et al. (1981) results were obtained from incoherent scatter

observations from 300-400 km, during several years of operation at Jicamarca.

Peru.

The results of Figure 8 come from a variety of methods, locations and

solar flux conditions, and contain a fair degree of experimental uncertainties.

Nevertheless, there is an encouraging agreement between the local time dependence

and magnitudes of the drifts obtained from the airglow imaging method and the

other traditional approaches to F-region dynamics. Theoretical considerations

suggest that nighttime plasma drifts near the equator should become approximately

equal to the F-region neutral winds which generate them via electrodynamic

dynamo action (Rishbeth, 1971, 1981; Heelis et al., 1974). The pattern of east-

ward speeds summarized in Figure 8 supports that view.

A close examination of well-defined features in Figures 5 and 6 (e.g.,

the wishbone formations) reveals that northward drift speeds are also evident

from the airglow images. These drifts are somewhat more difficult to extract

using overlay/grid techniques due to the inherent difficulty in trying to

identify small displacements in nebulous features. A few clearly-identified

cases were obtained, however, and they yielded northward speeds of $\approx$50 m/sec

from 22:00 to 23:00 L.T. During this time period, eastward speeds average

$\approx$130 m/sec, and thus a total horizontal ExB drift of $\approx$140 m/sec is consistent

with the declination of approximately 20° near Ascension Island.

4.4 Image Processing Techniques

The quality of photographs capable of being obtained from all-sky airglow

imaging suggests that computer processed photometric methods can be used to

extract detailed quantitative information from the photographs. In order to

test these procedures with our initial field data, the density distributions on

our 35 mm images were accessed using a two-dimensional scanning EIKONIX micro-

densitometer. The resulting digital output, formated to a 128x128 pixel array,

were converted to an intensity plane using well-known film calibration procedures.

Full details of the method have been described in Chapter 2.

In order to demonstrate the types of digital processing capable with a

relatively simple system, each 10-minute frame from two nights of observations

(1-2 and 2-3 February 1981) were digitized. The numerical average of all those

frames provided a simple way to characterize the average influences of the Van

Rhijn and vignetting effects, plus field contaminations, such as building lights

and telephone poles and wires. The subtraction of a single frame from the

average then yields a "difference picture" which, when added to a suitable

numerical offset, provides a very convenient way to characterize the fundamental

aspects of airglow depletions. Digital arrays such as these can then be
used to construct three-dimensional (x,y, intensity) airglow relief maps, and
associated two-dimensional contour plots. Figures 9 and 10 offer examples of
the technique. One can see that the method captures the essence of a photo-
graph, and provides the added benefit of quantitative intensity variations
free from geometrical, lens and field-of-view effects. The contours in
Figure 9, for example, show that the depths of the depletions decrease from
west to east, while in Figure 10, the wishbone depletion is seen as a continuous,
bifurcating formation extending several thousand kilometers from the geo-
magnetic equator. The grids in Figure 3 show that the left or eastern branch
of the wishbone is nearly parallel to a magnetic meridian, while the western
branch appears to be in the geographic north-south plane, as discussed earlier.
Figure 11 contains a schematic view of the 3-dimensional characteristics of
field-aligned depletions that could account for such an "airglow wishbone."

The digital arrays obtained from airglow images, such as in Figure 9
(1 February 1981 at 22:00 U.T.), can be used to examine the temporal evolution
of equatorial depletions in a high spatial resolution format. When an indivi-
dual frame is divided by the normalized composite average frame, the field of
view is corrected for van Rhijn and vignetting effects, and the depletions
appear as strong features on a relatively uniform background. An east-west
(or so-called prime-vertical) scan through the resultant array can then be
used to characterize the instantaneous cross sections of all the features in the
photograph. Figure 12 contains a series of 22 prime vertical scans, spanning
$3\frac{1}{2}$ hours of observations in 10-minute steps, from the night of 1-2 February 1981.
The pixel geometry along the east-west direction has been transformed into
a linear format in kilometers (at h = 300 km) in order to facilitate comparisons

of features photographed at zenith angles from 0 to 75 east and west.
Such a transformation removes the image compression effects that occur
towards the edge of a photograph. However, since the pixel spacing was
linear in the digitization process, the transformation to spatial coordinates
causes resolution to deteriorate badly at large zenith angles. Figure 12
therefore exhibits greatest detail within ±600 km of the zenith, with adequate
resolution for broad features out to ±1200 km (or a zenith angle of 75°).

The east-west airglow image scans in Figure 12 are plotted with successive
75-unit offsets on each side of the figure. The prime vertical scan from the
first photograph of the evening reveals a low level of airglow ($\simeq$25 units) that
is approximately uniform from east to west. As the F-region descends, back-
ground airglow and well-formed depletions emerge. The gradual east-west slope
in the background level reflects different local time regions across a
photograph (i.e., it is later and therefore brighter in the east). Peak back-
ground levels occur between 22:00-23:00 LT, showing approximately a 7-fold
increase over the levels recorded earlier in the evening. As the F-region
recombination mechanisms proceed towards midnight, background levels decrease
as bottomside plasma is consumed; the remnant background levels now remain
high towards the western horizon where the local time is still pre-midnight.
As seen in Figure 5, the prominant airglow depletions tend to disappear near
midnight.

Digitally processed image scans, as shown in Figure 12, can be used to
track individual depletions over their 3 to $3\frac{1}{2}$ hour residence time within the
all-sky field of view. For example, the depletion that appears near 700 km west
of Ascension Island at 20:40 LT drifts eastward with a speed of $\simeq$140m/sec at
21:00, crosses the zenith at $\simeq$120m/sec an hour later, and finally reaches 700 km

east of Ascension Island at 23:50 LT, for an average speed of ≈120 m/sec from west to east.

The prime vertical scans may also be used to describe the cross-sectional characteristics of individual airglow/plasma depletions. For example, the scan at 21:00 LT in Figure 12 depicts three depletions that are 2-2$\frac{1}{2}$ times less intense than the background level. The scan at 23:00 LT exhibits similar factor of 2 depletions upon a background that is now twice as bright as the 21:00 LT scan. Weber et al., (1980) reported depletions of similar magnitude using an airborne photometer to monitor zenith intensities of the drifting depletions. From Figure 12, it becomes clear that digital processing of all-sky images offers an attractive method of separating spatial and temporal changes, while still preserving the quantitative benefits of narrow beam photometer observations.

The east-west walls or longitudinal gradients on both sides of the depletions are particularly well defined in a series of prime vertical scans. In Figure 12, over 50 depletion cross-sections are shown from 22 photographs taken over a 3$\frac{1}{2}$ hour period. In the majority of cases, the 6300 $\overset{o}{A}$ intensity gradient on the western wall is sharper than the corresponding gradient on the eastern wall. Weber et al., (1980) have described a way of converting 6300 $\overset{o}{A}$ intensity to the average electron density within the airglow emission region, and thus the brightness gradients in Figure 12 should be good indicators of the actual bottom-side N_e gradients that define "plasma bubbles." The steepness history of a western wall is quite evident in the single, long-lived depletion described above; it appears on the western horizon in Figure 12 shortly before 21:00 LT transits the zenith near 22:00 LT, and passes to the eastern horizon after 23:00 LT. Throughout this period, the western wall is steeper than the eastern wall.

It should be noted, however, that the pronounced steepening of <u>both</u> walls as the depletion passes overhead in simply an effect a viewing geometry: at large zenith angles, the slant, integral measure of any trough-like feature will always characterize vertical walls as gradual boundaries in comparison to overhead observation of the same feature (a well-known problem encountered, for example, in attempts to measure the edges of the so-called mid-latitude ionospheric trough).

A final point to be mentioned with respect to Figure 12 concerns the intensity fluctuations that appear in the bright background levels near the zenith shortly before and after 23:00 LT. If characterized as enhancements upon a background, they appear as 20 increases in brightness, a value that is several times larger than the single pixel-to-pixel noise (~5) seen in the bright region near 21:00 LT. A 20 brightness variation is still too small to see on photographs printed to portray the factors of 2 to 3 difference found in depletion-to-background effects. The enhancements appear to be tens of kilometers in east-west extent, with lifetimes of tens of minutes. Further analysis is clearly required to determine if they are actual "fingers" or striations of enhanced plasma extending from the sharp western wall of the neighboring depletion, evidence of TID's in the airglow generating region, or some unknown problem associated with experimental or digitizing methods. For the present, where large-scale depletion characteristics are our main concern, it is best to consider these fluctuations as noise in the background levels that outline the depletions.

5. SUMMARY AND CONCLUSIONS

A new low-light-level, all-sky, airglow imaging system was developed to
carry out the first ground-based studies of the optical signatures of equatorial
plasma depletions. The basic contribution of the techniques rests on the
assumption that 6300 Å emission comes from a relatively narrow altitude range
in the bottomside F-region, and thus a region of depleted airglow represents the
base of a flux tube with severely depleted plasma content. A narrow band of
depleted airglow extending away from the equator therefore relates to a
series of depleted flux tubes that cross the equator at increasingly greater
heights.

A two-week field test of the optical system designed to conduct equatorial
airglow depletion studies was carried out on Ascension Island in early 1981.
The initial results to come from these observations may be summarized as follows:

1. Airglow depletions were observed on 70 of the clear nights. They appeared
   after 20:00 LT, occurred most abundantly during the 20:30 - 23:30 LT
   period, and disappeared after midnight. On the average, they covered
   approximately one-fourth of the sky for at least two hours.

2. The depletions often extended from the magnetic equator to beyond the
   crest of the southern intertropical arc (3000 km). Individual depletions
   had east-west cross sections of 100 to several 100 km.

3. The airglow depletions were aligned in a variety of directions, all with
   approximate north-south orientations. In most cases, depletions were
   not aligned with a magnetic meridian, but rather showed a progressive
   skewness to the west at further distances from the equator.

4. Several cases of apparently twisting, overlapping and bifurcating deple-
   tions were observed.

5. The depletions drifted to the east with speeds that decreased from
   ~190 m/sec at 21:00 LT to ~80 m/sec at 01:00 LT.

6. Airglow intensities within depletions were typically 40-50 of the
   background intensities that defined them.

7. The western wall of a depletion usually had a steeper gradient than
   the corresponding eastern wall.

8. Possible evidence exists for small regions (~10 to 50 km) of enhanced
   airglow embedded in the bright background areas between depletions.

The results outlined above support and extend the conclusions reached in the

initial series of equatorial airglow depletion morphologies obtained by weber

et al., (1978, 1980) and Moore and Weber (1981). The airglow imaging technique

may also be used for high resolution, quantitative investigations of depletion

characteristics by using relatively simple image processing methods. This

approach is most useful for extracting specific spatial and temporal parameters

related to the mechanisms responsible for the equatorial depletion effects.

   Zalesak et al, (1982) have recently presented a comprehensive review of

their numerical simulation studies of the nonlinear evolution of the gravita-

tionally-driven, collisional Rayleigh-Taylor instability considered responsible

for equatorial plasma bubbles. Their simulation results contain many features

reported in earlier experimental work, especially incoherent scatter observations

from Jicamarca (Woodman and LaHoz, 1976) and Kwajalein (Tsunoda, 1980). The radar

results are often depicted in maps of meter-size irregularity characteristics as

a function of space and time. The simulations are not aimed at these small-

scale perturbations, but rather at the large-scale (100's km) characteristics

of the envelopes or boundaries of the small scale effects. The optical results

presented here have a spatial extent and scale length that are more closely

related to the simulation results carried out to date. Several large-scale

perturbation results computed by Zalesak et al., such as depletion widths, tilts.
bifurcations and steep west wall gradients below hmax, are all evident in the
data set described here. Further detailed comparisons of simulation results and
airglow imaging data may prove useful in understanding the complex processes
that control the evening, equatorial ionosphere.

REFERENCES

Aarons, J., and H.E. Whitney, Recent observations of equatorial and high latitude scintillations, AGARD. Conf. Proceed. No. 284, Propogation Effects in Space/Earth Paths, NATO/AGARD, Neuilly Sur Seine, France, 1980.

Anderson, D.N., Modeling the ambient, low latitude F-region ionosphere-- a review, J. Atmos. Terr. Phys., 43, 753, 1981.

Anderson, D.N. and R.G. Roble, Neutral wind effects on the equatorial F-region ionosphere, J. Atmos. Terr. Phys., 43, 835, 1981.

Babier, D., G. Will, and J. Glaume, L'emission de la raie ronge du ciel nocturne en Afrique, Ann. Geophys., 17, 305, 1961.

Bates, D.R., The origin of the night sky light, Mon. Not. Roy. Astron. Soc., 106, 509, 1946.

Baumgardner, J., and J.A. Klobuchar, All-sky camera images of 6300 Angstrom airglow depletions as indicators of regions of strong L band scintillation, private communication, 1981.

Cabannes, J., Les raies rouges de l'oxygene dans le spectre du ciel nocturne, C.R. Acad. Sci., 200, 1905, 1935.

Chamberlain, J.W., Physics of the Airglow and Aurora, Academic Press, New York, 1961.

Fejer, B.G., D.T. Farley, C.A. Gonzales, R.F. Woodman, and C. Calderon, F-region east-west drifts at Jicamarca, J. Geophys. Res., 86, 215,

Hays, P.B., D.W. Rusch, R.G. Roble and J.C.G. Walker, The OI(6300 Å) airglow, Rev. Geophys. Space Sci., 16, 225, 1978.

Heelis, R.A., P.C. Kendall, R.J. Moffett, D.W. Windle, and H. Rishbeth, Electric coupling of the E and F regions and its effect of F-region drifts and winds, Planet. Space Sci., 21, 743, 1974.

Matsushita, S., B.B. Balsley and H. Rishbeth, Preface to papers from the sixth international symposium on equatorial aeronomy, J. Atmos. Terr. Phys., 43, 375, 1981.

McClure, J.P., W.B. Hanson, and J.F. Hoffman, Plasma bubbles and irregularities in the equatorial ionosphere, J. Geophys. Res., 82, 2650, 1977.

Mende, S.B., and R.H. Eather, Monochromatic all-sky observations and auroral precipitation patterns, J. Geophys. Res., 81, 3771, 1976.

Mende, S.B., R.H. Eather, and E.K. Aamodt, Instrument for the monochromatic observation of all sky auroral images, Appl. Opt., 16, 1691, 1977.

Mendillo, M., J. Baumgardner, and H. Spence, Airglow imaging studies of natural and artificially induced ionospheric disturbances, Tech. Report, in press, Air Force Geophys. Lab, Bedford, MA 01730, 1982.

Moore, J.G. and E.J. Weber, OI6300 and 7774 A airglow measurements of equatorial plasma depletions, J. Atmos. Terr. Phys., 43, 851, 1981.

Peterson, V.L., T.E. Van Zandt and R.B. Norton, F region nightglow emissions of atomic oxygen, 1, Theory, J. Geophys. Res., 71, 2255, 1966.

Rishbeth, H., The F-layer dynamo, Planet. Space. Sci., 19, 263, 1971.

Rishbeth, H., The F-region dynamo, J. Atmos. Terr. Phys., 43, 387, 1981.

Sipler, D.P. and M.A. Biondi, Equatorial F-region neutral winds from nightglow OI 630.0nm Doppler widths, Geophys. Res. Lett., 5, 373, 1978.

Sipler, D.P., M.A. Biondi, and R.D. Hake, Optical studies in support of the July 1979 Kwajalein equatorial spread-F campaign, DNA Tech. Rep. 5528P, 1 Nov. 1980, Defense Nuclear Agency, Washington, D.C. 20305.

Tsunoda, R.T., On the spatial relationship of 1-m equatorial spread F irregularities and plasma bubbles, J. Geophys. Res., 85, 185, 1980.

Weber, E.J., J. Buchau, R.H. Eather, and S.B. Mende, North-south aligned equatorial airglow depletions, J. Geophys. Res., 83, 712, 1978.

Weber, E.J., J. Buchau, and J.G. Moore, Airborne studies of equatorial F layer ionospheric irregularities, J. Geophys. Res., 85, 4631, 1980.

Woodman, R.F., and C. La Hoz, Radar observations of F region equatorial irregularities, J. Geophys. Res., 81, 5447, 1976.

Zalesak, S.T., S.L. Ossakow, and P.K. Chaturvedi, Nonlinear equatorial Spread F: the effect of neutral winds and background Pederson Conductivity, J. Geophys. Res., 87, 151, 1982.

FIGURE CAPTIONS

Figure 1. Schematic view of low-light-level camera system developed for equatorial airglow depletion studies.

Figure 2. Location of Ascension Island with respect to geographic and geomagnetic coordinate systems. The two concentric rings mark the "all-sky" camera coverage for zenith distances of 75 and 90°, respectively. The heavy dashed lines mark dip latitudes of ±15 , giving the approximate locations of the crests of the equatorial (Appleton) anomaly and their associated intertropical airglow bands. Several equatorial observing sites are shown in relation to Ascension Island.

Figure 3. Sample photograph showing equatorial airglow depletions embedded in a weak background of 6300 Å emission, together with three scale-size grids giving geographic, geomagnetic and zenith angle parameters. Note the inverted east-west directions, the markers for telephone poles in the field of view, and 3 zenith angle calibrations on each of the grids.

Figure 4. Magnetic meridional geometry across the equatorial region near Ascension Island, and its relationship to airglow features recorded in all-sky photographs. (see text.)

Figure 5. A series of 6300 Å photographs taken at 10-minute intervals during the night of 7-8 February 1981. (see text for discussion.)

Figure 6. Examples of all-sky images of 6300 Å airglow features recorded at 20-minute intervals. The top panel (1 February 1981) shows the motion of three narrow depletions towards the northeast, while the lower panel (2 February 1981) shows an example of a "wishbone" airglow depletion. The bright background levels highlight the telephone poles and wires that serve as convenient orientation markers; two buildings with rooftop lights obscure a small portion of the eastern horizon. Resolution limits may be estimated by the widths of the wires and the combined images of Jupiter and Saturn (the bright elongated feature that moves towards the west, close to the equator, from the building lights on the eastern horizon.)

Figure 7. Summary of airglow depletion extent with respect to the visible airglow from Ascension Island (from Baumgardner and Klobuchar, 1981).

Figure 8. Average eastward drift of airglow features versus local time, derived from all-sky images recorded from January to February 1981. The number of individual drifts used to form the average speeds appear in parentheses. Eastward speeds measured by other techniques and at other locations are shown for comparison. (see text.)

Figure 9. Example of digital processing results for the all-sky, 6300 Å airglow image recorded at 22:00 UT on 1 February 1981. The three-dimensional relief map uses a "difference from the mean" technique to correct for lens and field of view effects; the two-dimensional

contour of the airglow map shows depletion effects with contours
of relative intensity (see text).

Figure 10.   Example of digital image processing upon the "wishbone" forma-
             tion recorded in the 6300 Å airglow image recorded at 00:30 UT on
             3 February 1981. (see Figure 6 and text.)

Figure 11.   Schematic representation showing how a wishbone-shaped equatorial
             airglow depletion maps along geomagnetic field lines to outline
             plasma depletion characteristics above the equator.

Figure 12.   A series of east-west ("prime-vertical") scans from the digital
             arrays created from the 22 photographs of 6300 Å airglow images
             recorded on the night of 1 February 1981. The data are corrected
             of vignetting and van Rhijn effects, and converted to east-west
             distances assuming a mean height of 300 km for the airglow emission.
             The scans at 20:00 LT (bottom left) and 22:10 (bottom right) are
             plotted in relative intensity units, with 10 subsequent scans plotted
             with successive 75 unit offsets.

INTENSIFIED CAMERA SYSTEM

60°LENS

180°LENS

24mm DIAMETER FIELD LENS

F/2.8 COLLIMATOR LENS

INTERFERENCE FILTER
(1 OF 4)

F/2.8 OBJECTIVE LENS

25mm 2nd GENERATION
IMAGE INTENSIFIER

F/1.2 COLLIMATOR AND
OBJECTIVE LENSES

35mm SLR CAMERA WITH
250 EXPOSURE BACK
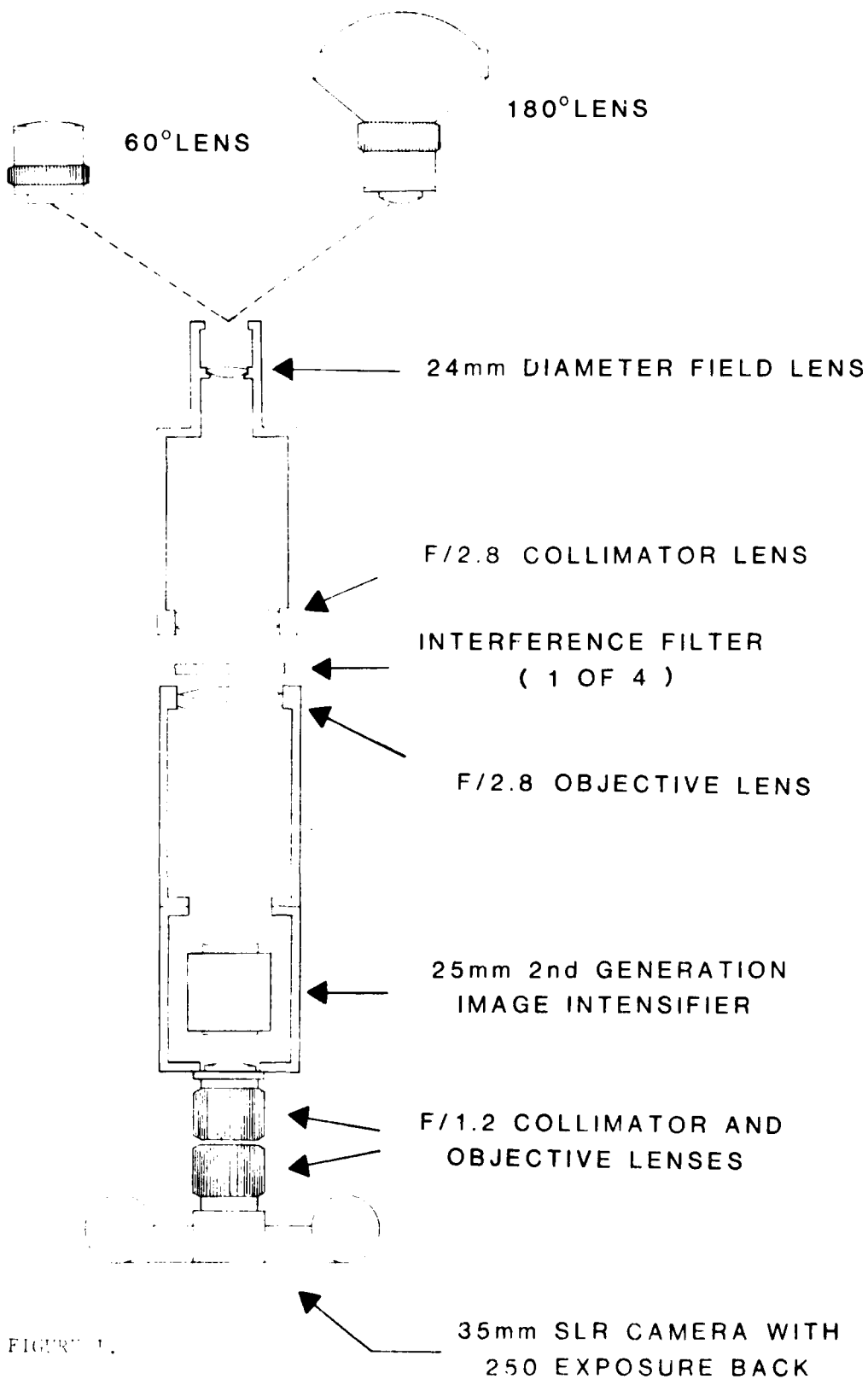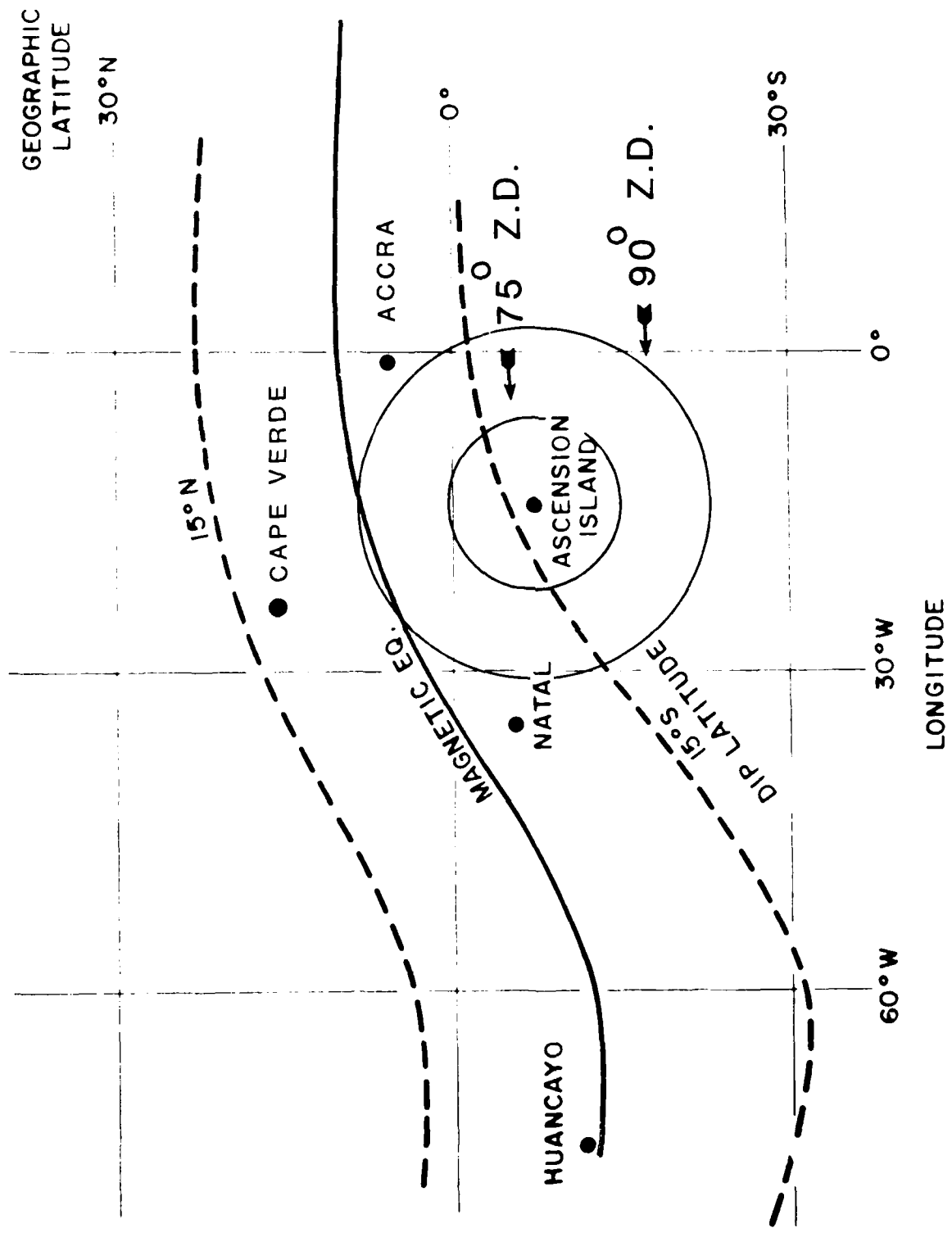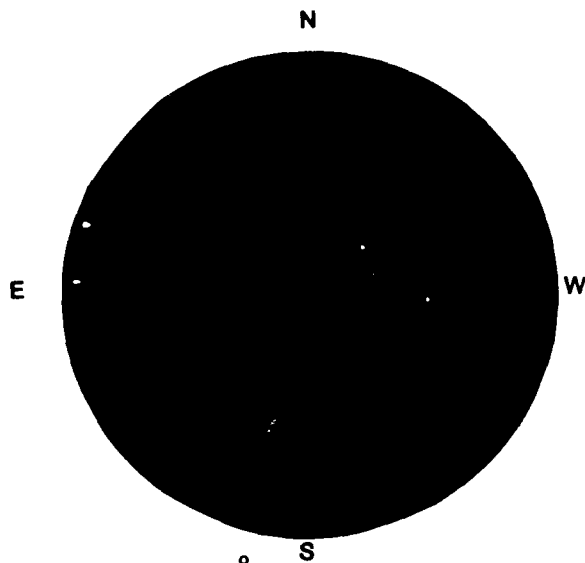
FIGURE 1.

FIGURE 2.

**6300 Å AIRGLOW IMAGE
FROM ASCENSION ISLAND**
(30 JANUARY 1981 22:20 UT)
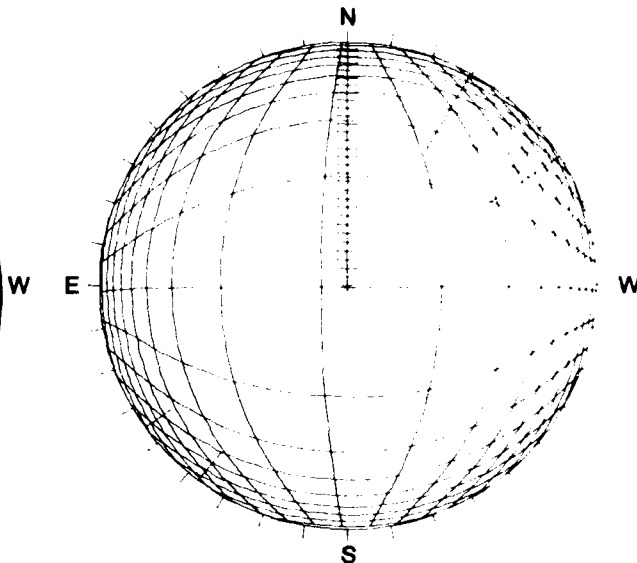
**GEOGRAPHIC GRID FOR 300 km
MERIDIANS AT 2° INTERVALS**
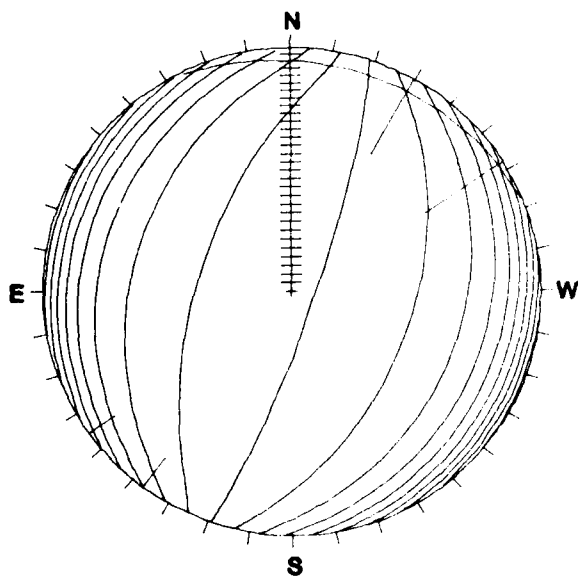
**MAGNETIC GRID FOR 300 km
MERIDIANS AT 2° INTERVALS**
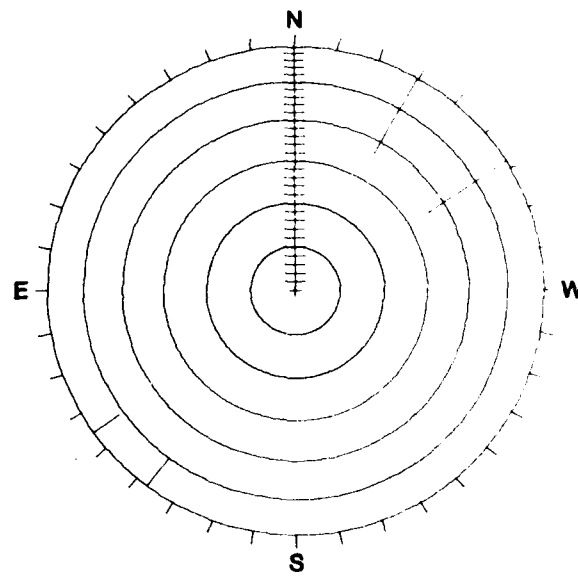
**ZENITH ANGLE GRID
15° INTERVALS**

FIGURE 3.

ASCENSION ISLAND MAGNETIC MERIDIAN
AIRGLOW VIEWING GEOMETRY
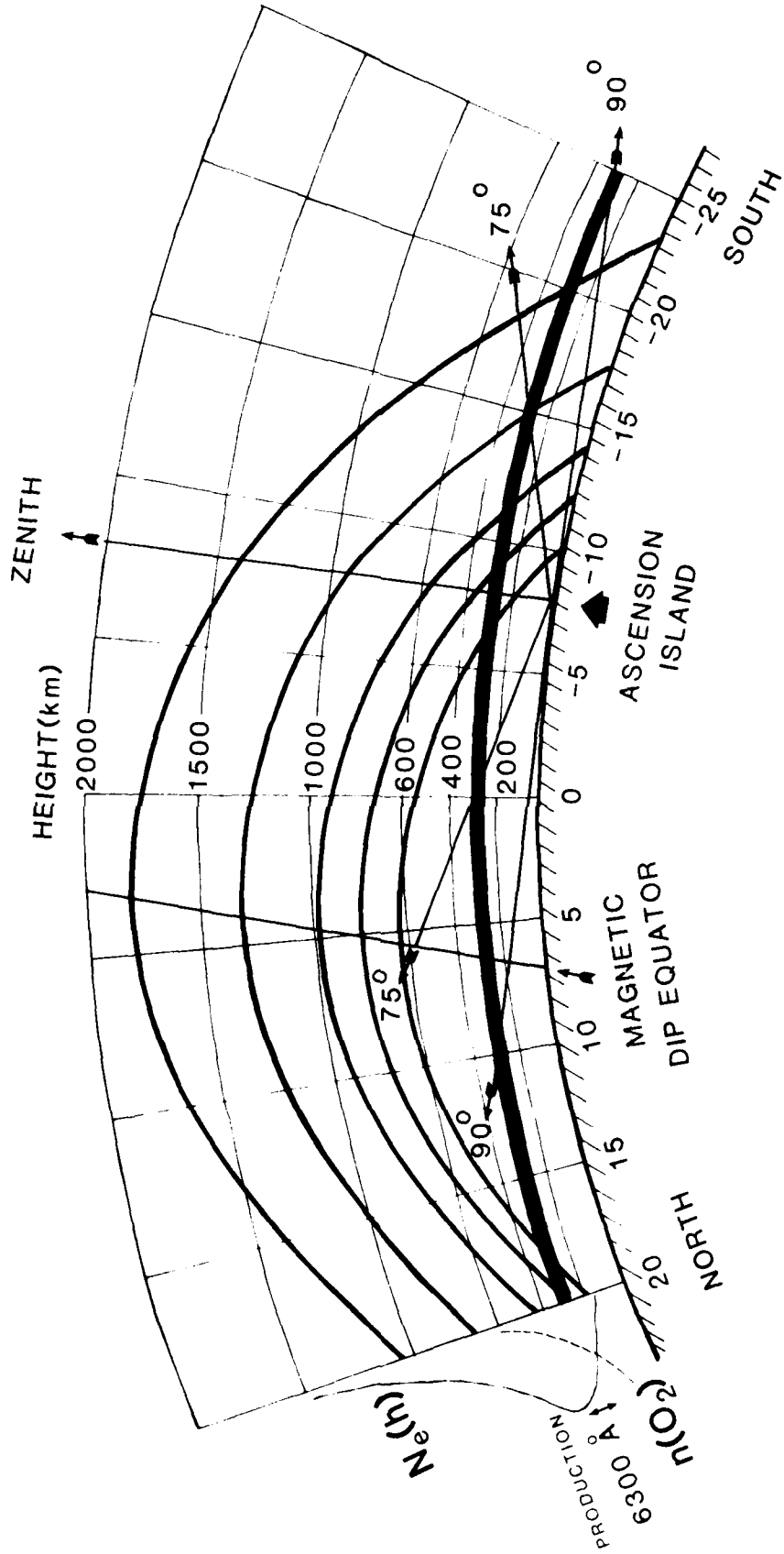
FIGURE 4.
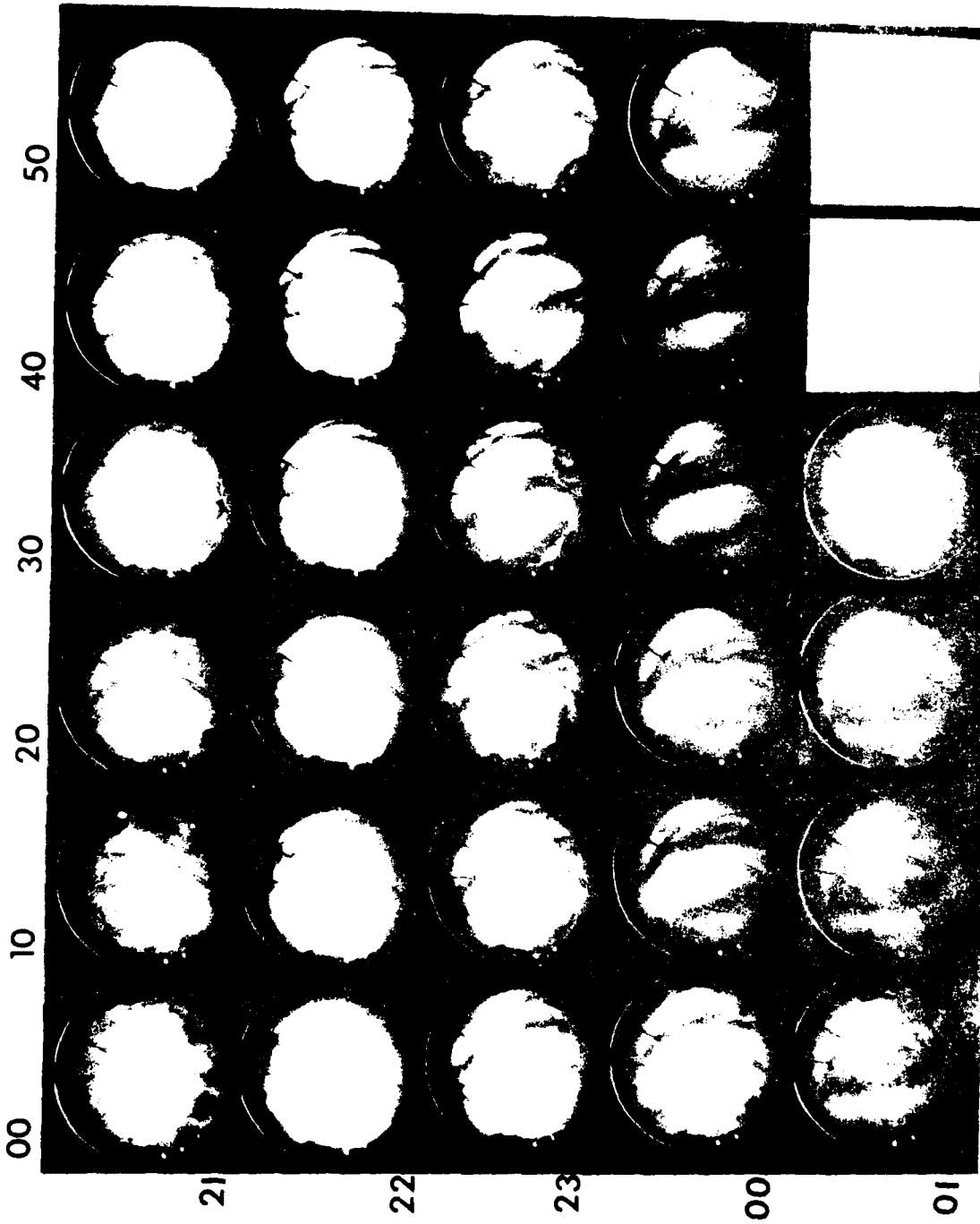
6300 Å ALL-SKY IMAGES FROM ASCENSION ISLAND

8 FEBRUARY 1981

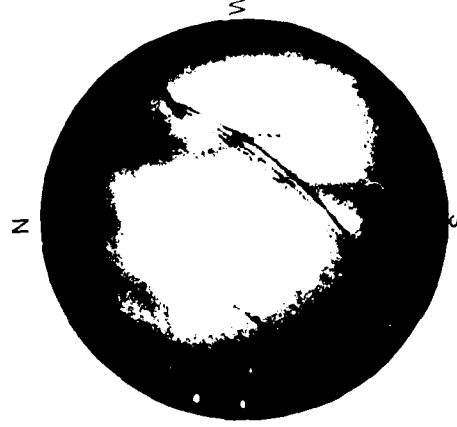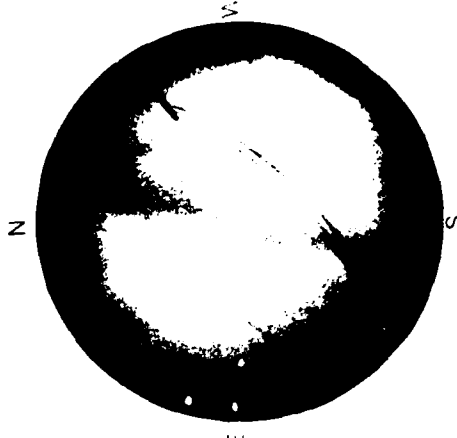ASCENSION ISLAND 6300 Å IMAGES — FEBRUARY 1981
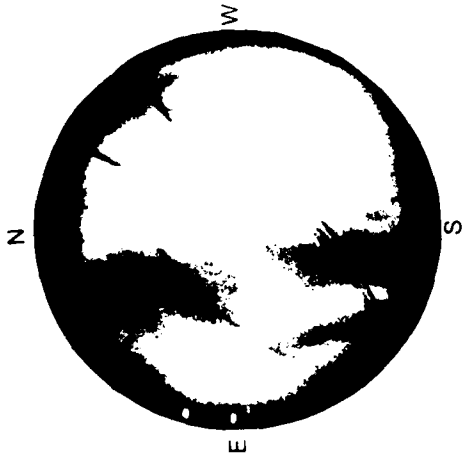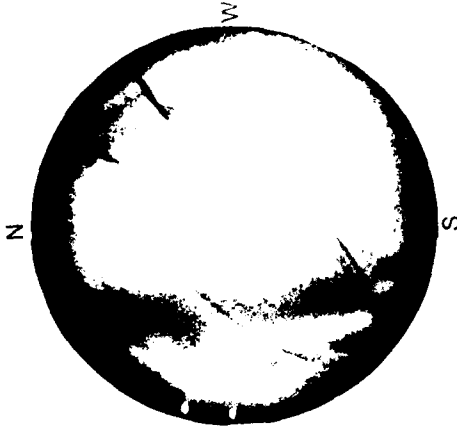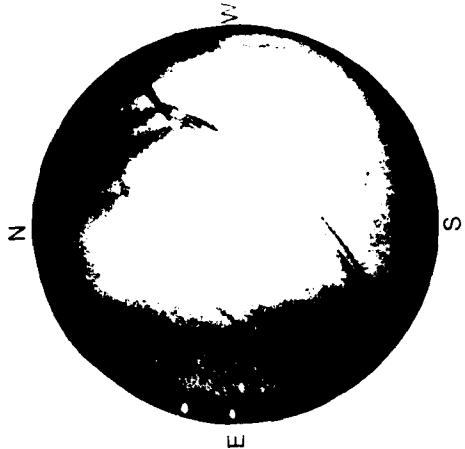
1 FEB 22:30 L.T.   22:50   23:10
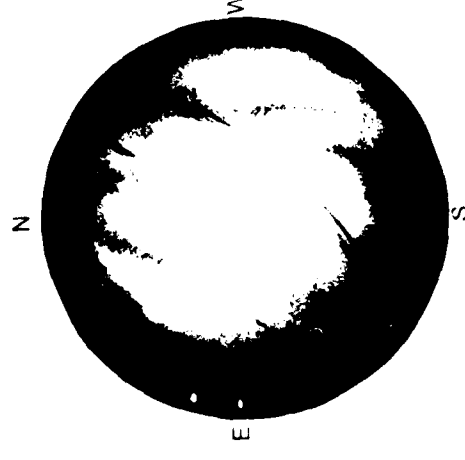
2 FEB 23:00 L.T.   23:20   23:40

FIGURE 6.

ASCENSION ISLAND JAN – FEB 1981
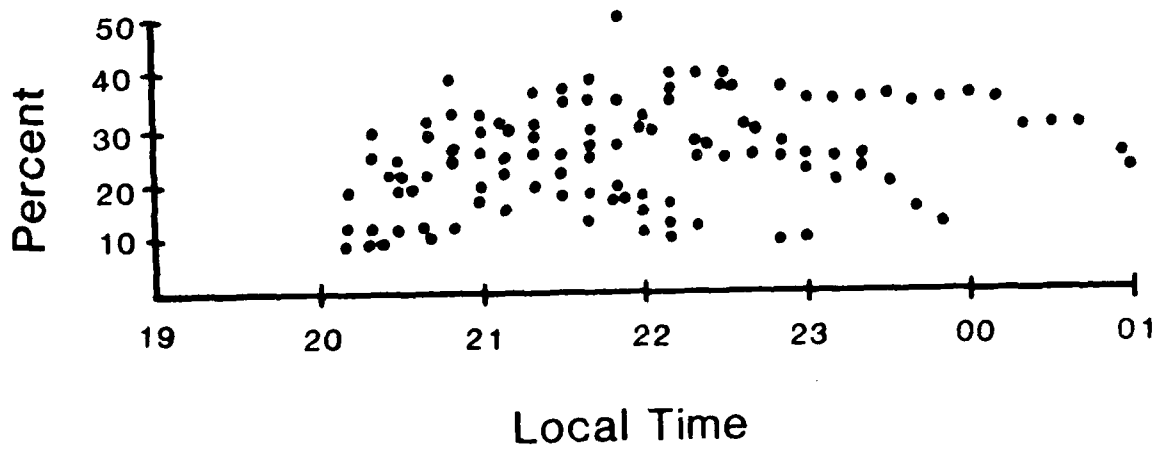Percentage of Visible Sky Covered
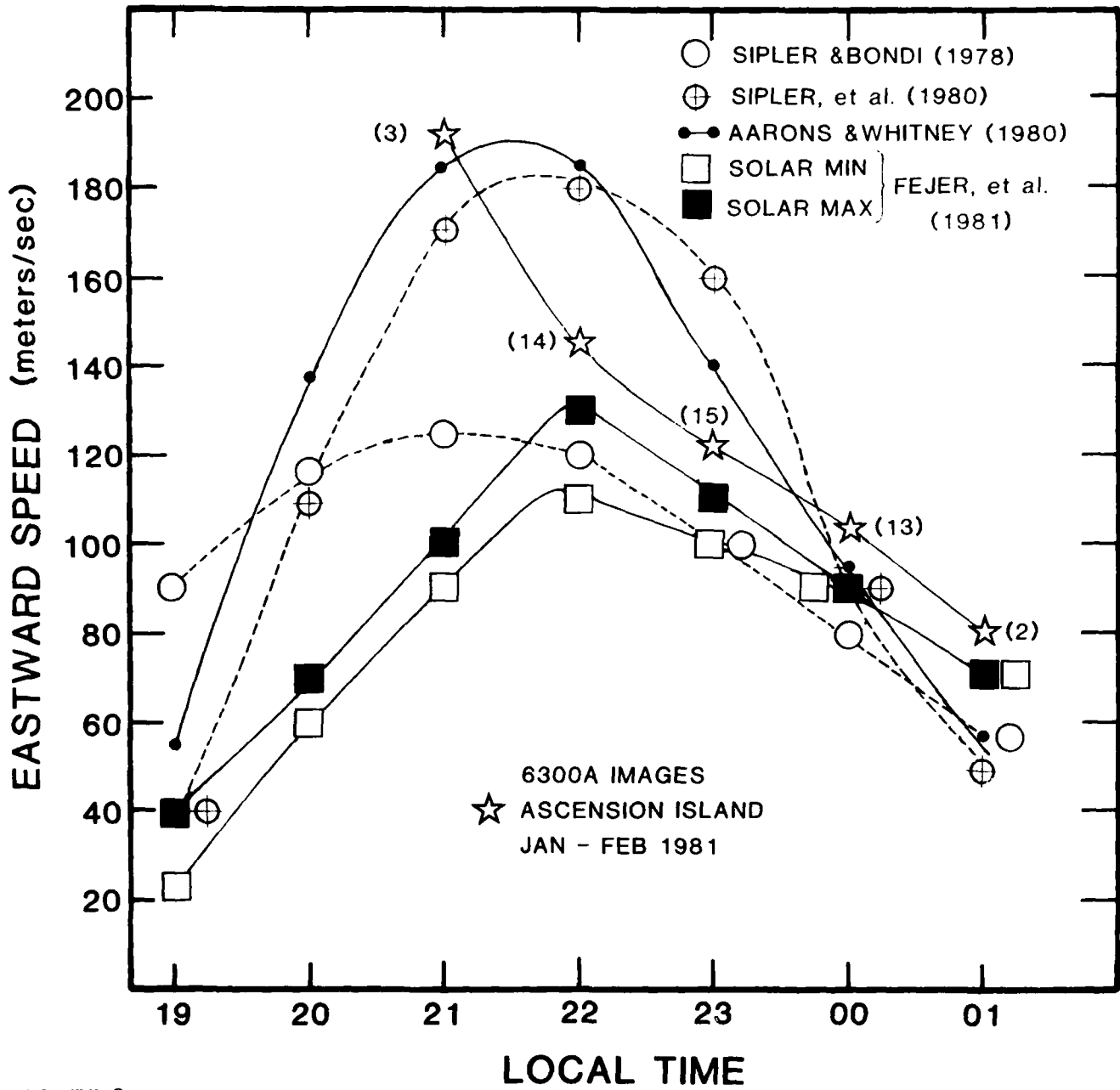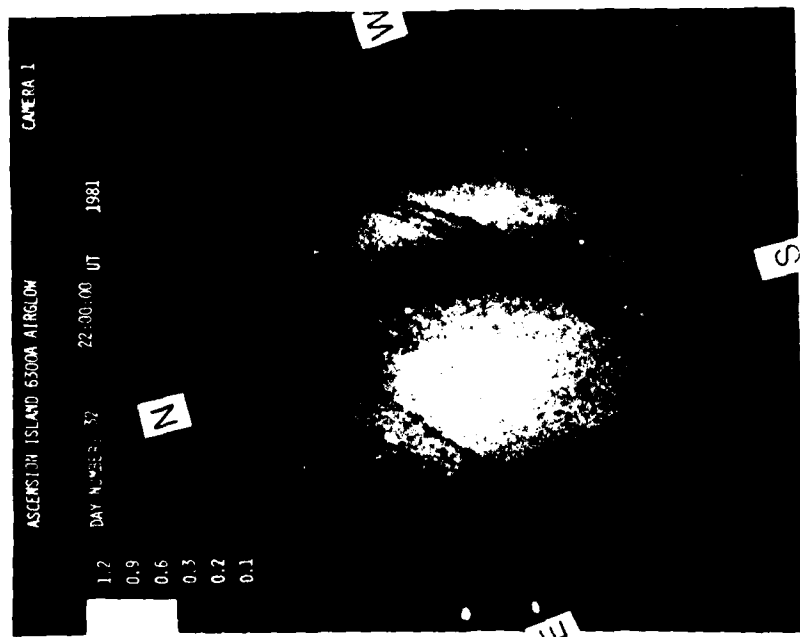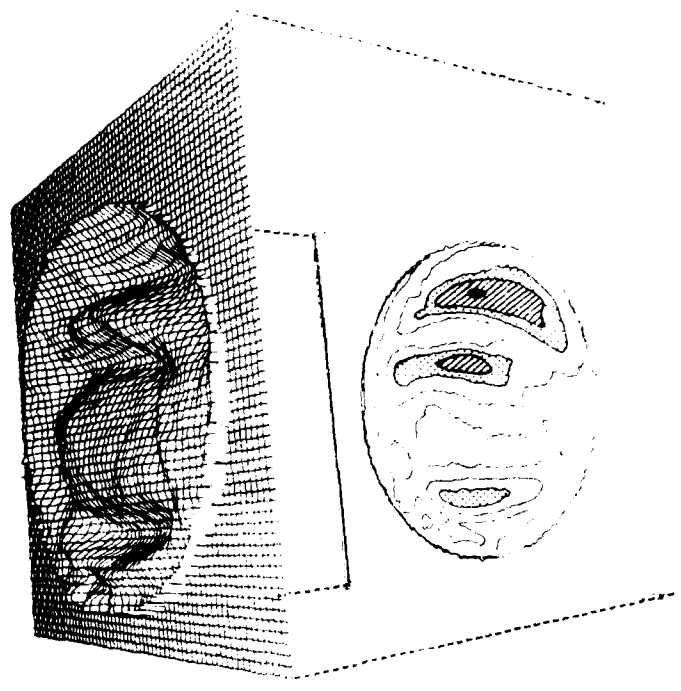by 6300Å Airglow Depletions

FIGURE 7.

FIGURE 8.

ASCENSION ISLAND 6300 Å AIRGLOW

22:00 U.T.
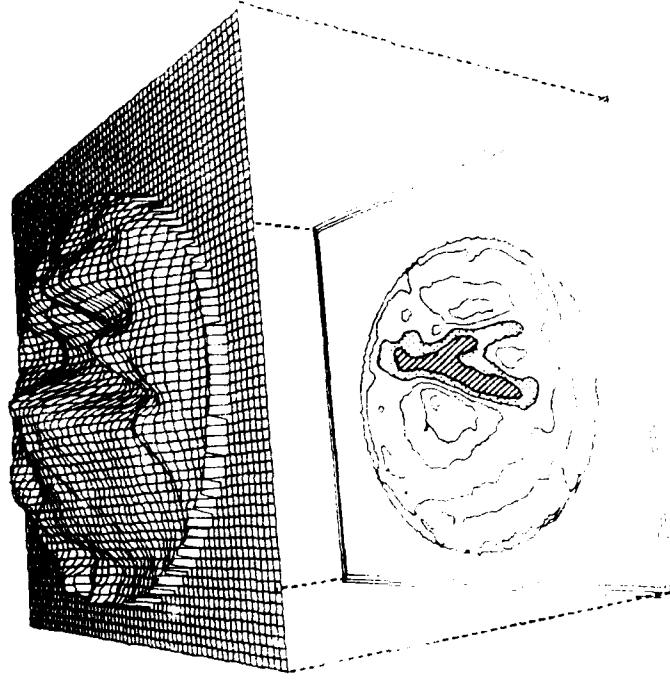
ASCENSION ISLAND 6300A AIRGLOW   22:00.00 UT   1981

DAY NUMBER 32

CAMERA 1

N
W
S
E

1.2
0.9
0.6
0.3
0.2
0.1

1 FEBRUARY 1981

FIGURE 6.

ASCENSION ISLAND 6300 Å AIRGLOW

00:30 U.T.

3 FEBRUARY 1981

HEIGHT (KM)
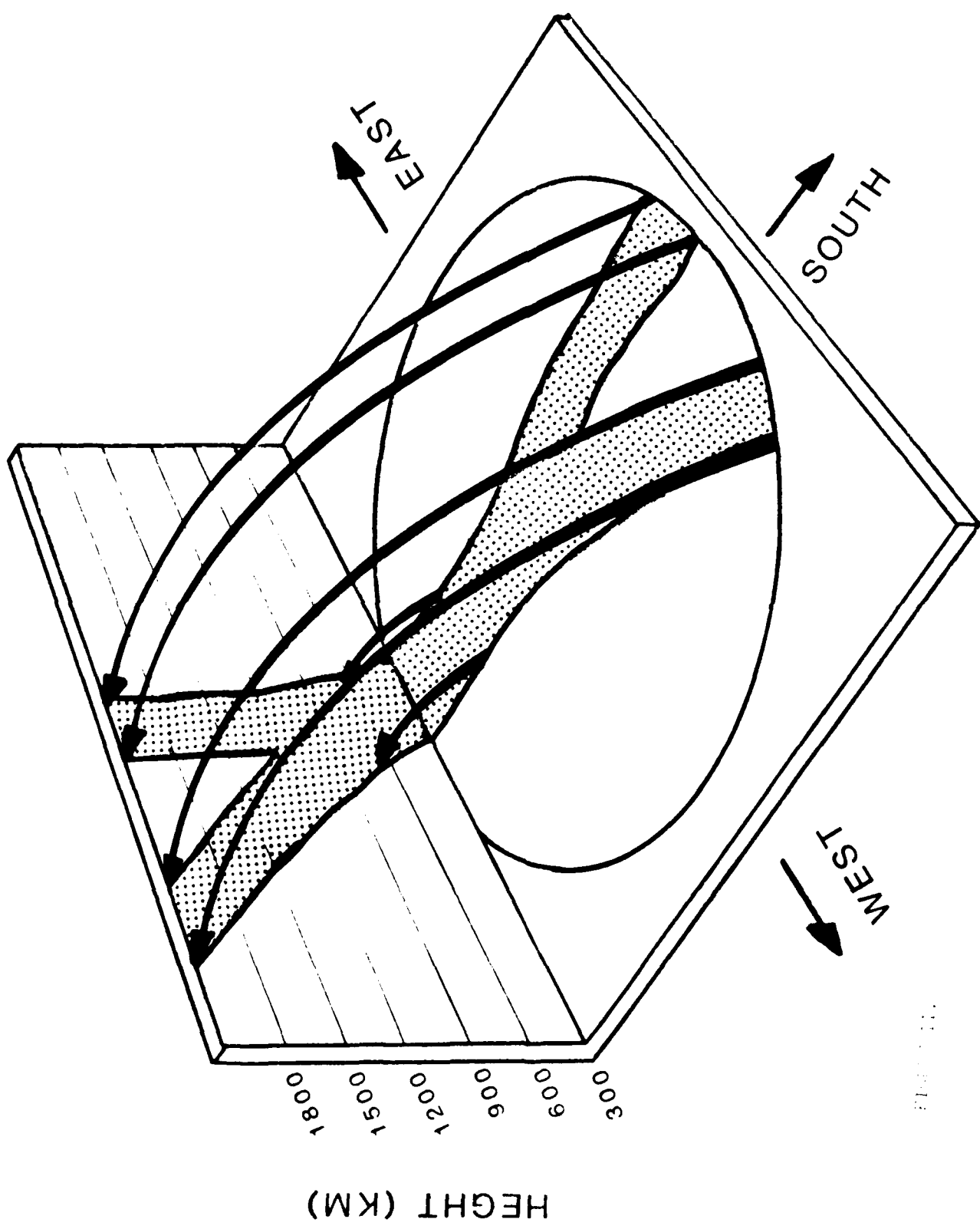
6300 A AIRGLOW IMAGE SCANS

ASCENSION ISLAND
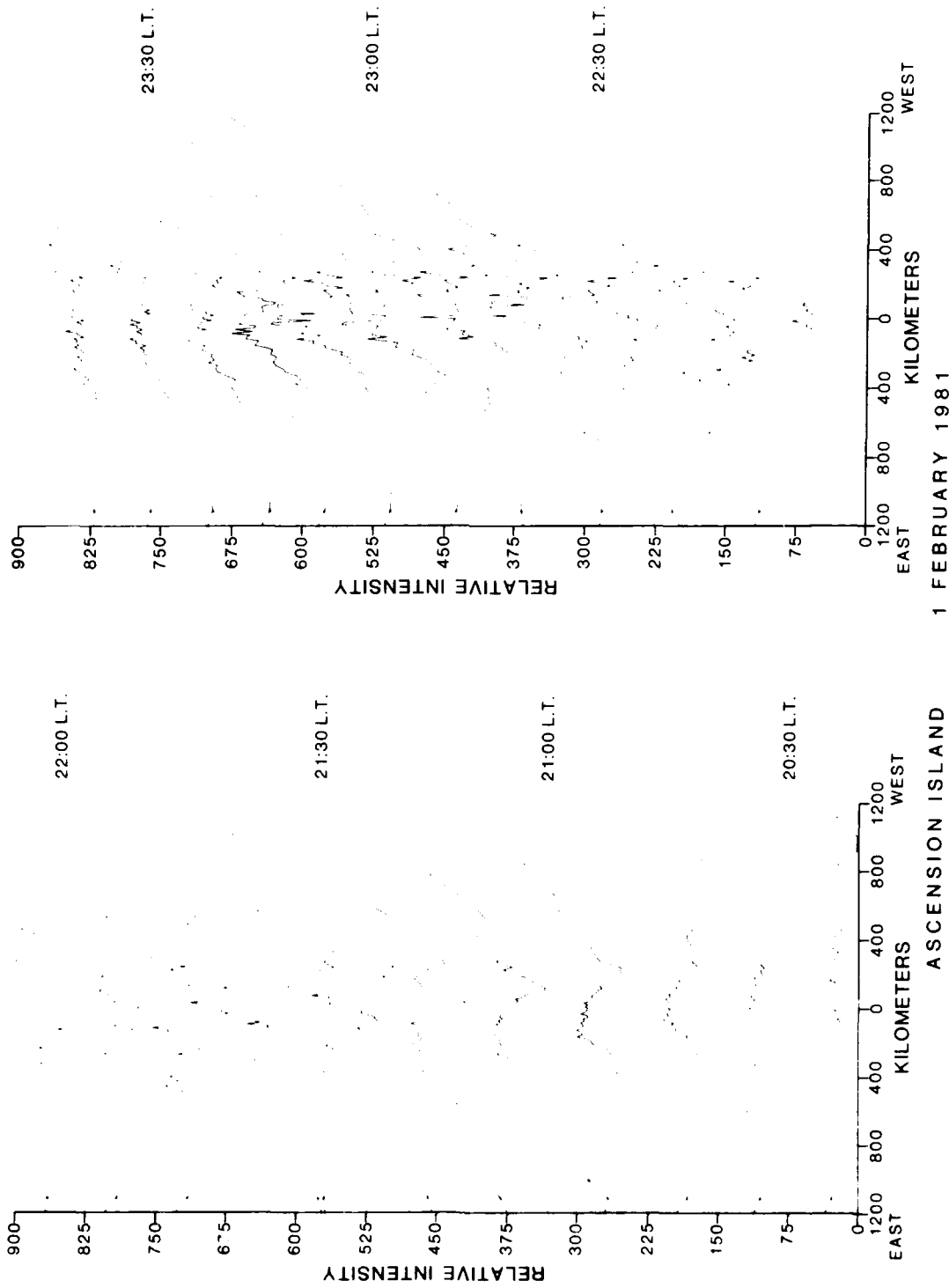
1 FEBRUARY 1981

FIGURE 12.

OPTICAL SIGNATURE OF AN IONOSPHERIC HOLE

INTRODUCTION

Rocket exhaust induced effects upon the ionosphere are a form of laboratory-in-space experimentation that can be used to address a broad range of chemical and dynamical processes of interest to aeronomic and space plasma research (Mendillo, 1981). While radio diagnostic systems have been the main technique to monitor such effects (Mendillo et al, 1975, 1980), optical methods can provide a complimentary way of observing disturbance morphologies (Kofsky et al, 1980; Stone and Zinn, 1980). A recent rocket launch provided a new "experiment of opportunity" to test the utility of low light level, image intensified photography as a diagnostic tool for ionospheric modification experiments.

The NOAA-C weather satellite was launched at 10:53 U.T. from Vandenberg Air Force Base (34.6°N, 120.6°W) on 23 June 1981. The Atlas-F launch vehicle followed a rarely used ascent profile that called for an engine burn well into the topside F-region (see Figure 1). A temporary observing station was established near Edwards Air Force Base (35.0°N, 117.8°W) to make radio beacon and optical measurements of the anticipated effects. The site was chosen in order to have the ray path of the 136 MHz beacon from ATS-1 pass through the rocket's exhaust plume at 350 km. The VHF radio beacon was used to measure the total electron content (TEC) along the ray path by the standard Faraday rotation technique (Titheridge, 1972). The site was also selected on the basis of clear sky conditions in order to provide the first opportunity to make optical measurements along the same path as a TEC-detected hole.

The optical system consisted of a photometer with a 1° field of view and a low light level imaging system with interchangeable all-sky (180°) and narrow-field (60°) lenses. The imaging system records intensified output on 35 mm film using a conventional single lens reflex camera. All observations were made using 6300 Å filters that have a very narrow half-power width (6 Å), a condition made necessary by the presence of the third quarter moon. Control data were taken at 6200 Å and the photometer records were reduced to absolute values using a calibrated source. The narrow field data reported on here were obtained using 8 second exposures.

RESULTS

Figure 2 contains a summary of the electron content and photometer measurements made during the event. The Faraday rotation data show a very rapid depletion of the F-region followed by a burst of airglow from the oxygen line at 6300 Å. Figure 3 presents a sample of the imaging results using the 60° field of view lens. Note
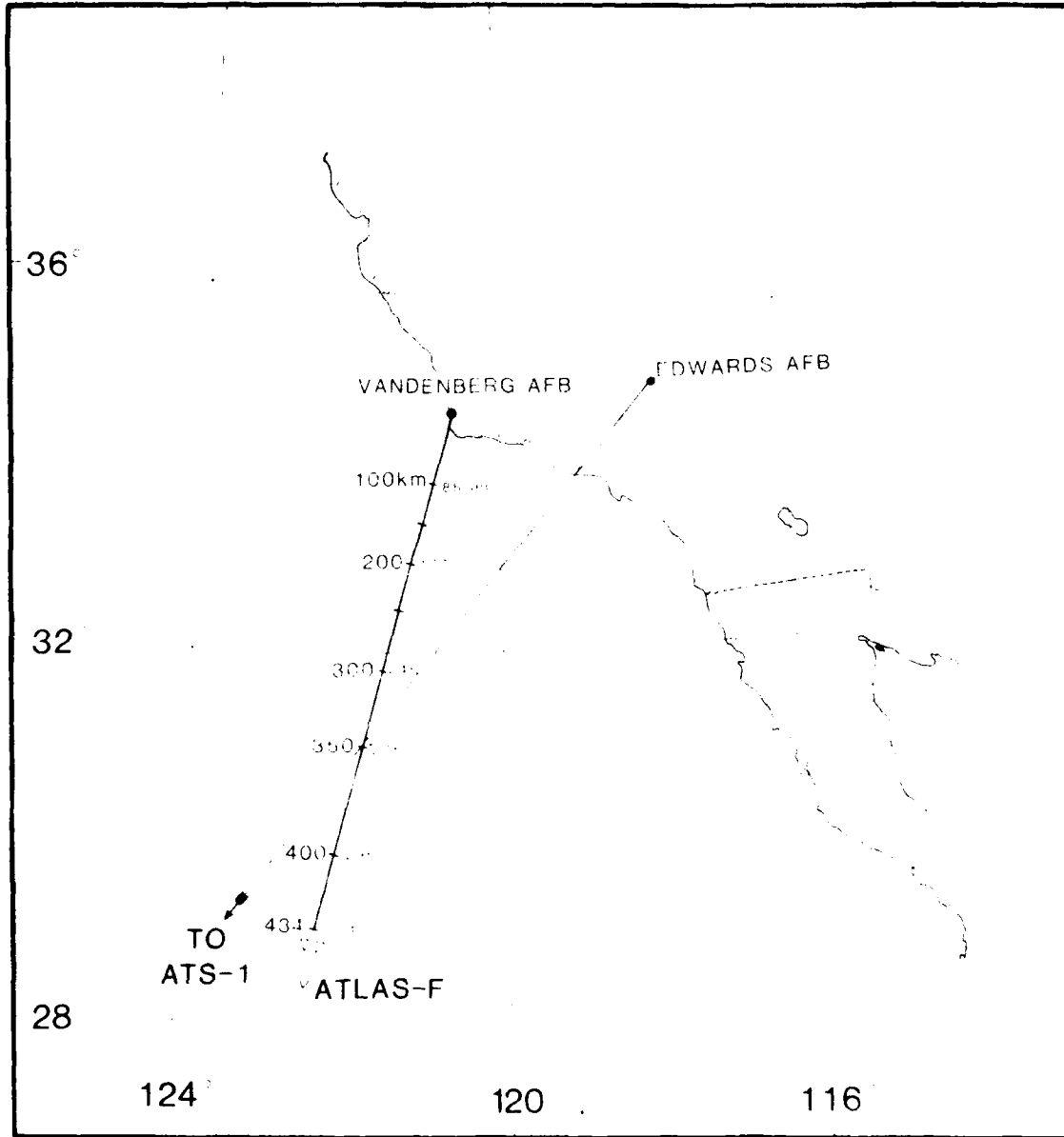
NOAA-C LAUNCH   23 JUNE 1981

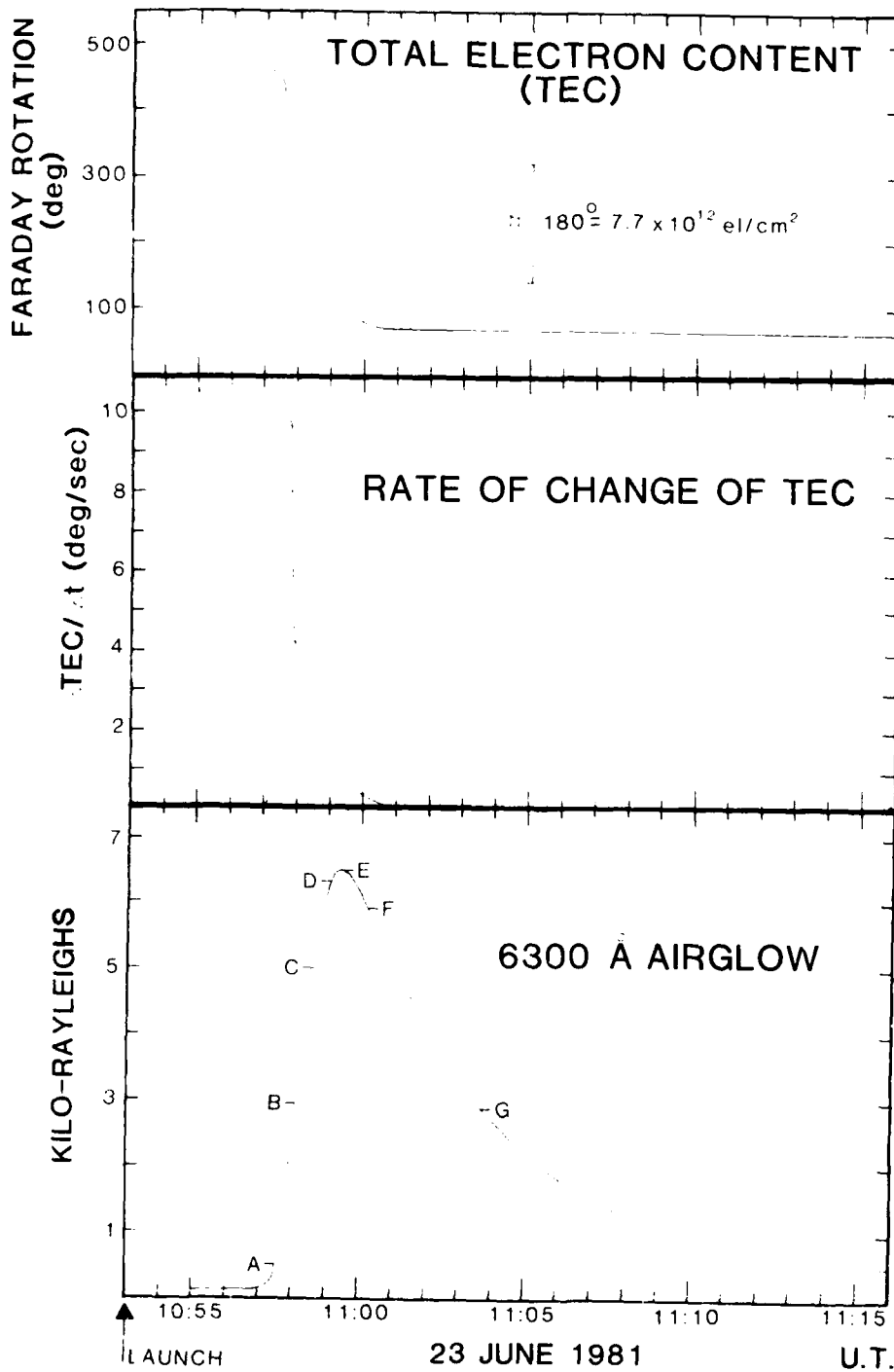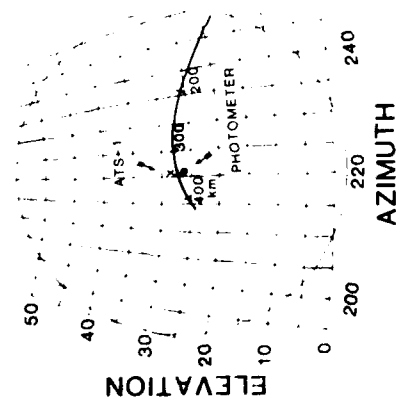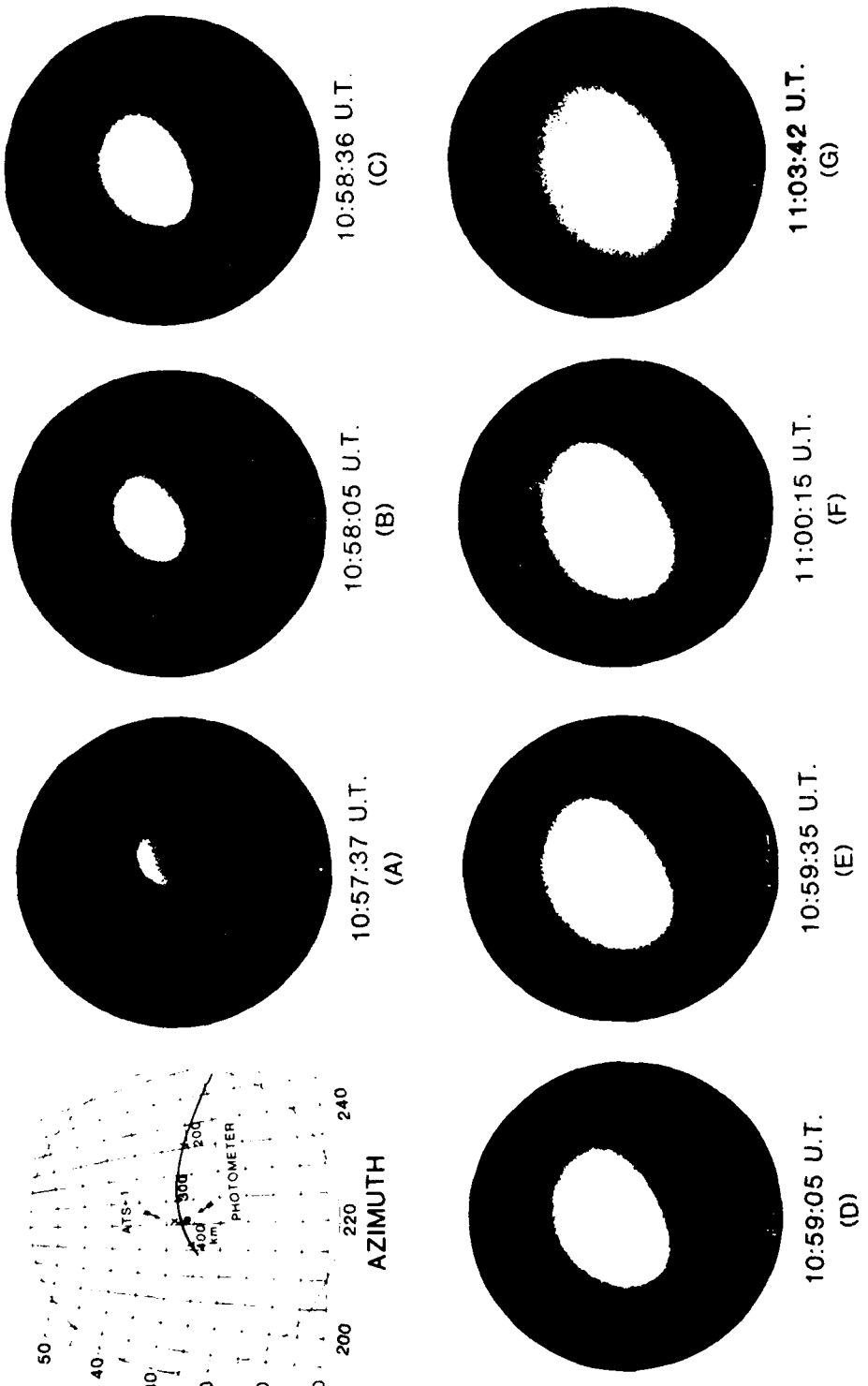FIGURE 1. ATLAS-F trajectory and observing site locations.

FIGURE 2. Electron content and photometer observations (uncorrected for atmospheric extinction). Letters A through G mark times of intensified images given in Figure 3.

the position of the photometer monitoring point, the ATS-1 point, and the times
of the photographs in relation to the photometric curve in Figure 2. The images
in Figure 3 show that a "smoke-ring" or "horseshoe-shaped" wave of airglow expand-
ed with the cloud of exhaust molecules responsible for the F-region depletions.
This effect is described in more quantitative fashion in Figure 4. Digital pro-
cessing of the images was carried out by scanning a 512 x 512 array on an EIKON-
IXSCAN 7800 system. These data were corrected subsequently for lens effects and
smoothed to the 128 x 128 pixel array contoured in Figure 4. The horseshoe pat-
tern is quite evident on a log (Intensity) format, and the lowest level contour
($\log I = 1.5 \simeq 100$ R) gives a good representation of the outermost visible edge
on the photograph. The full evolution of this contour level provides an overall
summary of the spatial and temporal development of the airglow pattern (see Figure 5).

DISCUSSION

Rocket exhaust clouds typically include molecules of H_2, H_2O and CO_2. These
gases react with the dominant F-region ion (O^+) to form molecular ions (OH^+, H_2O^+,
H_3O^+, O_2^+) at rates 100 to 1000 times faster than the normal O^+ reactions with
atmospheric O_2 and N_2. The end result is that an atomic ion plasma is converted
to a molecular ion plasma that can recombine quickly with electrons. Since the
rocket plume diffuses rapidly through the F-region, the enhanced recombination
process occurs over a broad altitude range and a columnar electron content deple-
tion is observed. The dissociative recombination reactions that cause the hole
can leave atomic oxygen atoms in excited states and thus to a burst of airglow.
Theoretical models for hole-making/airglow scenarios have been described by
Anderson and Bernhardt (1978) and Zinn and Sutherland (1980).

Measurements reported here of the evolving airglow cloud can be used to test
various chemical, diffusive and optical parameters related to plasma modification
mechanisms. Two aspects are addressed in this preliminary analysis: diffusion
and airglow production.

FIGURE 3. Intensified 6300 Å photographs using a 60° field lens.

23 JUNE 1981

10:57:37 U.T.
(A)

10:58:05 U.T.
(B)

10:58:36 U.T.
(C)

10:59:05 U.T.
(D)

10:59:35 U.T.
(E)

11:00:15 U.T.
(F)

11:03:42 U.T.
(G)

ELEVATION

AZIMUTH

ATS-1

PHOTOMETER
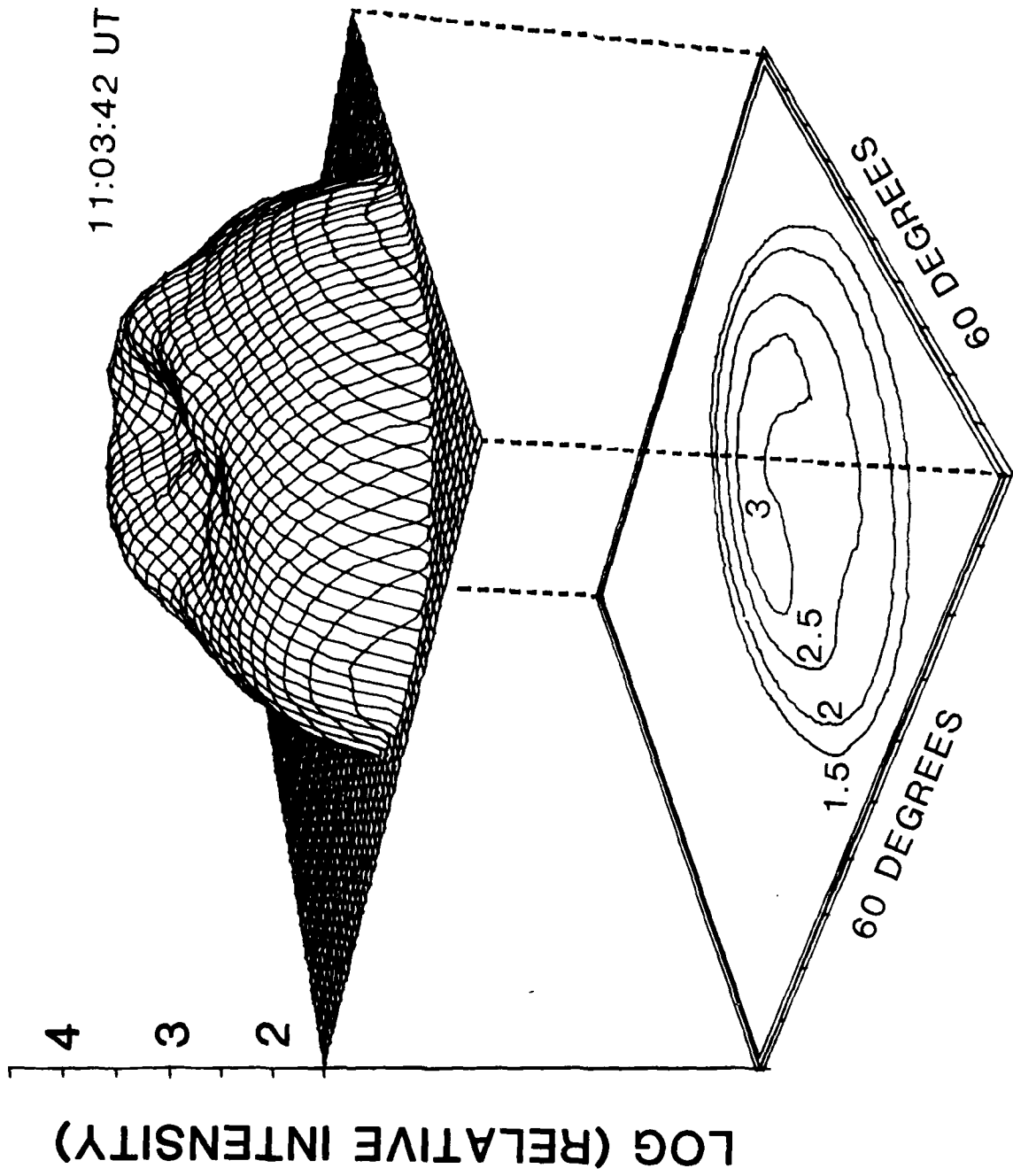
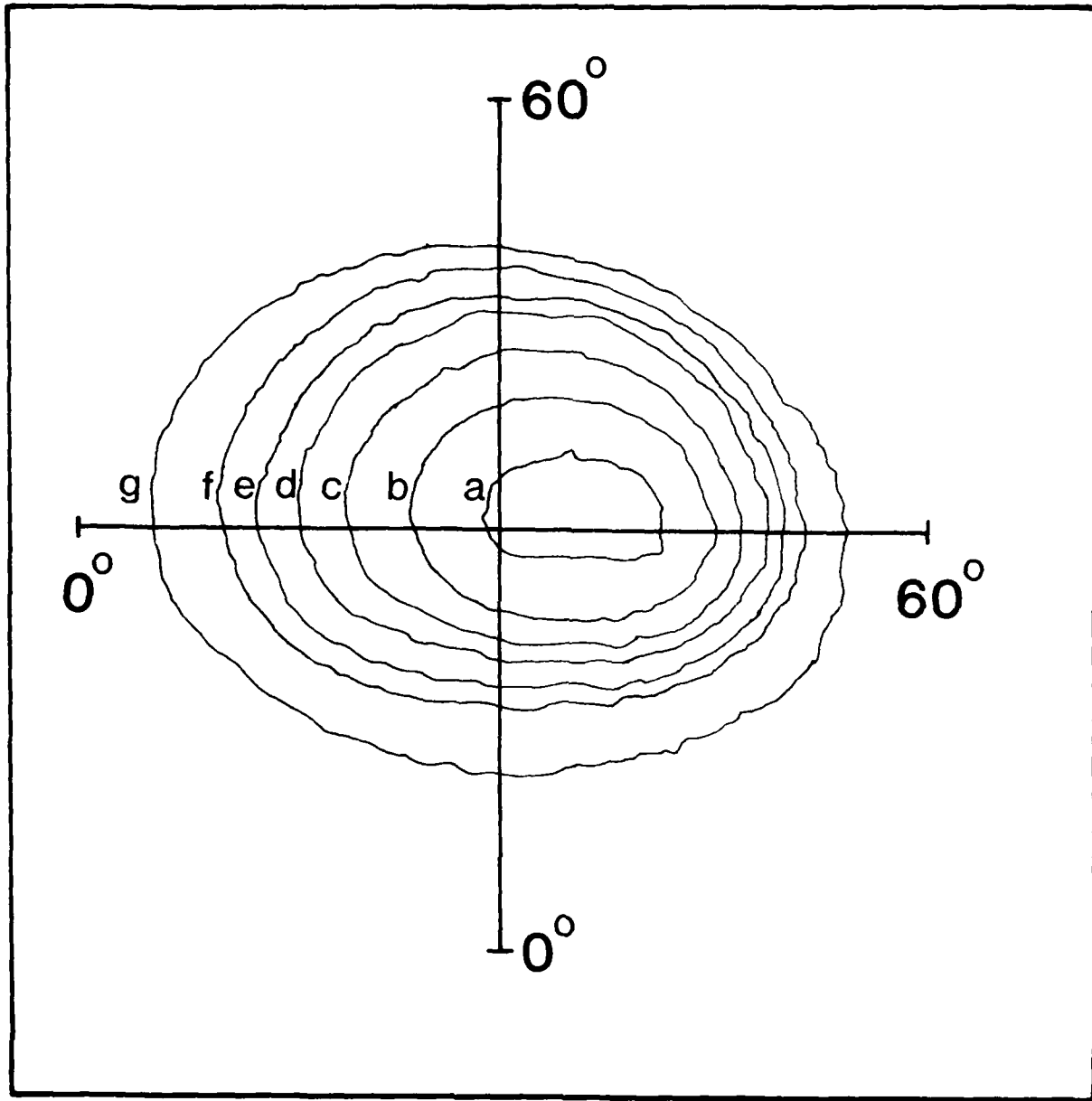Figure ... of Radio spectrum 6400 Å taken from frame (6) in Figure 3.

FIGURE 5. Summary of outermost isophote (Log I = 1.5) for all frames in Figure 3.

1. Diffusion. The diffusion of modification related gases in the
F-region has been treated by Bernhardt et al. (1975), Mendillo and
Forbes (1978), Schunk (1978), and Bernhardt (1979). Since the injected
molecules react quickly with the ambient ions, and the 6300 Å emission occurs
with the subsequent dissociative recombinations, the expanding airglow pattern
should be related to time constants associated with molecular diffusion. Using
a simple diffusion model, one can show that the time of peak 0^+ loss (t_{max}) is
related to distance (r) from an initial source as $t_{max} = r^2/6D$,
where D is the diffusion coefficient for the injected molecules (Mendillo et al.,
1975).

The composite contours in Figure 5 are not spherical due to the horizontal
motion of the rocket and the exponential nature of the background atmosphere.
Nevertheless, they can be used to set an upper limit for diffusion using
equivalent spherical arguments. Figure 6 gives the effective linear expansion
rates along the major and minor axes of the contours, together with a
theoretical equivalent spherical growth rate using $D = 30 \times 10^{10}$ cm^2/sec.
This value is consistent with the diffusion of the lightest species (H_2) through
background oxygen at 350 km and $T = 1000^\circ K$.

2. Relationship between hole formation and 6300 Å airglow emission.

The exhaust gases of an Atlas-F rocket include the following molecular injec-
tion rates (in units of 10^{26} molecules/sec): $OH = 1.5$, $H_2 = 3.6$, $CO_2 = 4.0$ and
$H_2O = 10.2$. Current models of hole formation show that the production
of the $O(^1D)$ state of oxygen is related directly to the dissociative
recombination of molecular ions (OH^+, O_2^+, H_2O^+) formed by these molecules. The
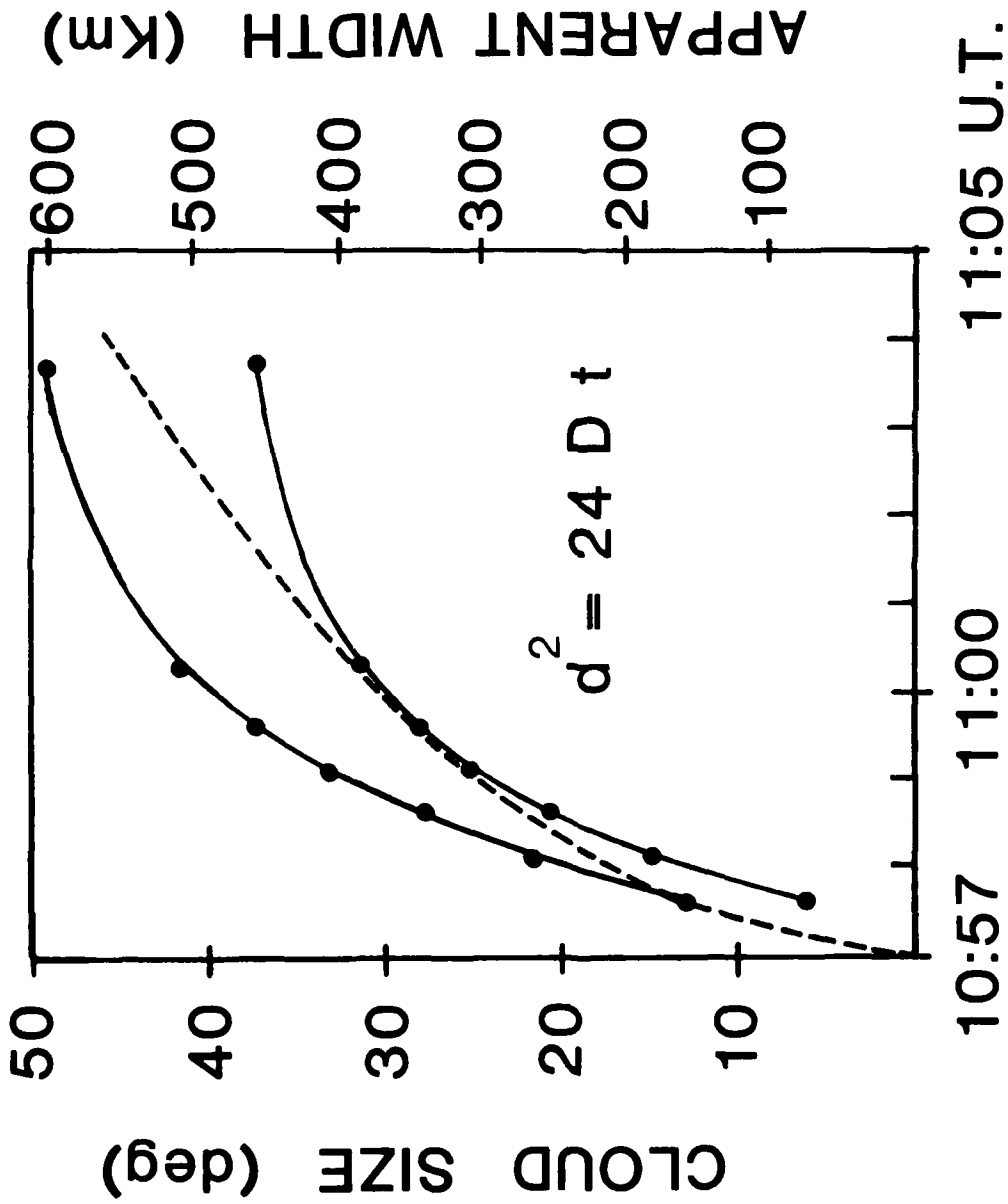emission of 6300 Å photons is described by the Einstein coefficient A_1 for the

Figure 6. Comparison of expansion rates in Figure 5 with equivalent spherical diffusion model results (see text).

$^1D \rightarrow {}^3P_2$ transition and the column content of the ^1D state, $[O*]_T$.

$$E_T = A_1 \int [O*] \, dh = A_1 [O*]_T \frac{photons}{cm^2 \, sec} = A_1 \times 10^{-9} [O*]_T \, kR \qquad (1)$$

For the unperturbed ionosphere, steady-state conditions are usually invoked and $[O*]_T$ is computed by first balancing production and loss at each height (see, e.g., Forbes, 1970). Since a modification scenario is inherently non-steady-state, such an assumption may not be used here; it is possible, however, to use height-integrated quantities to make a simple estimate of the time dependence of $[O*]_T$. Thus, if motions are neglected,

$$\frac{d[O*]_T}{dt} = P - L = -k \frac{dN_T}{dt} - (A_T + Q_T) [O*]_T. \qquad (2)$$

The first term represents the column production rate of O*, where k is the column-averaged fraction of plasma recombinations that yield the excited $O(^1D)$ state, and dN_T/dt is the observed rate of change of the columnar electron content. The loss term derives from the total ^1D emission rate, A_T ($^1D \rightarrow {}^3P_0, {}^3P_1, {}^3P_2$), and Q_T is the effective total columnar quenching rate. Since ΔN_T was observed to decrease exponentially with an effective loss coefficient, β, equation (2) may be written as

$$\frac{d[O*]_T}{dt} = k\beta\Delta N_T e^{-\beta t} - (A_T + Q_T) [O*]_T \qquad (3)$$

The solution to (3), when coupled to (1), yields

$$E_T(t) = \frac{A_1 \, k\beta\Delta N_T \times 10^{-9}}{(A_T + Q_T - \beta)} [e^{-\beta t} - e^{-(A_T + Q_T)t}] \qquad (4)$$

The coefficients A_1 and A_T are fixed at 0.0069 sec^{-1} and 0.0091 sec^{-1}, while ΔN_T and β are obtained from the observations in Figure 2: $\beta = 0.0213$ sec^{-1} and $\Delta N_T \simeq 16.8 \ 10^{12}$ el/cm^2. The average branching ratio k for the number of 0* per recombination and the column average quenching coefficient Q_T can assume a range of values in equation (4). Three pairs of (k-Q_T) solutions to (4) are plotted in Figure 7, with each case chosen to yield the observed peak 6300 Å emission corrected for atmospheric extinction:

$$E_T \ (t_{max}) = 8.9 \text{ kR at } t_{max} = \frac{\ln[(A_T + Q_T)/\beta]}{(A_T + Q_T - \beta)} \qquad (5)$$

It becomes clear from Figure 7 that the best agreement between the observed and computed $E_T(t)$ curves occurs for the no-quenching case. With $Q_T = 0$, t_{max} from (5) occurs 70 seconds after the initiation of the ΔN_T decrease; the observations in Figure 2 show that the peak emission occurred nearly 120 seconds after the onset of the hole. Quenching of 0* by molecular species is of the form $Q_T = \gamma[\overline{XY}]$, where $[\overline{XY}]$ is the average molecular concentration within the hole and γ is approximately 5×10^{-11} cm^3/sec (Forbes, 1970; Roble et al., 1976). For a 1000 °K neutral atmosphere (CIRA, 1972), N_2 at 350 km is $\simeq 2 \times 10^7$ cm^{-3} and thus $Q_T \simeq 0.001$ sec^{-1} or only 10% of A_T in equation (5). The exhaust molecules themselves could be effective quenchers, especially H_2O (Hudson and Reed, 1979). This could be important at early times, when concentrations $\sim 10^7$ cm^{-3} are required to account for the β derived above. Nevertheless, the condition $Q_T \simeq 0$ in equation (4) may well be a reasonable first approximation for estimating the 6300 Å airglow to come from an ionospheric hole formed in the upper F-region. Under such conditions, approximately 14% of the recombinations yield $0(^1D)$ atoms. For significantly higher quenching rates, proportionately larger yields of 0* per recombination are required. Such adjustments to equation (4) cause the peak emission to occur at yet earlier times and the decay to ambient levels occurs much faster than observed.
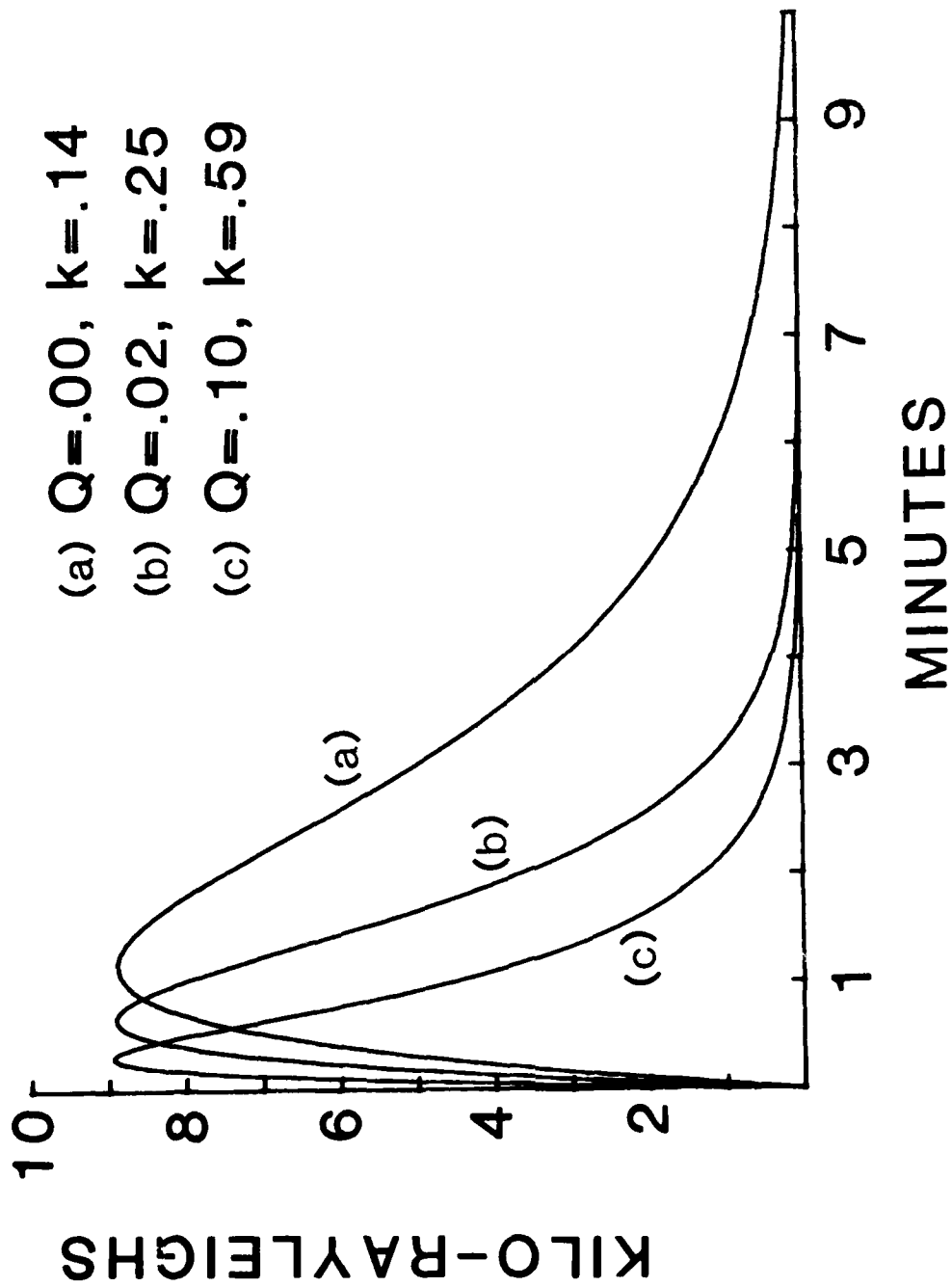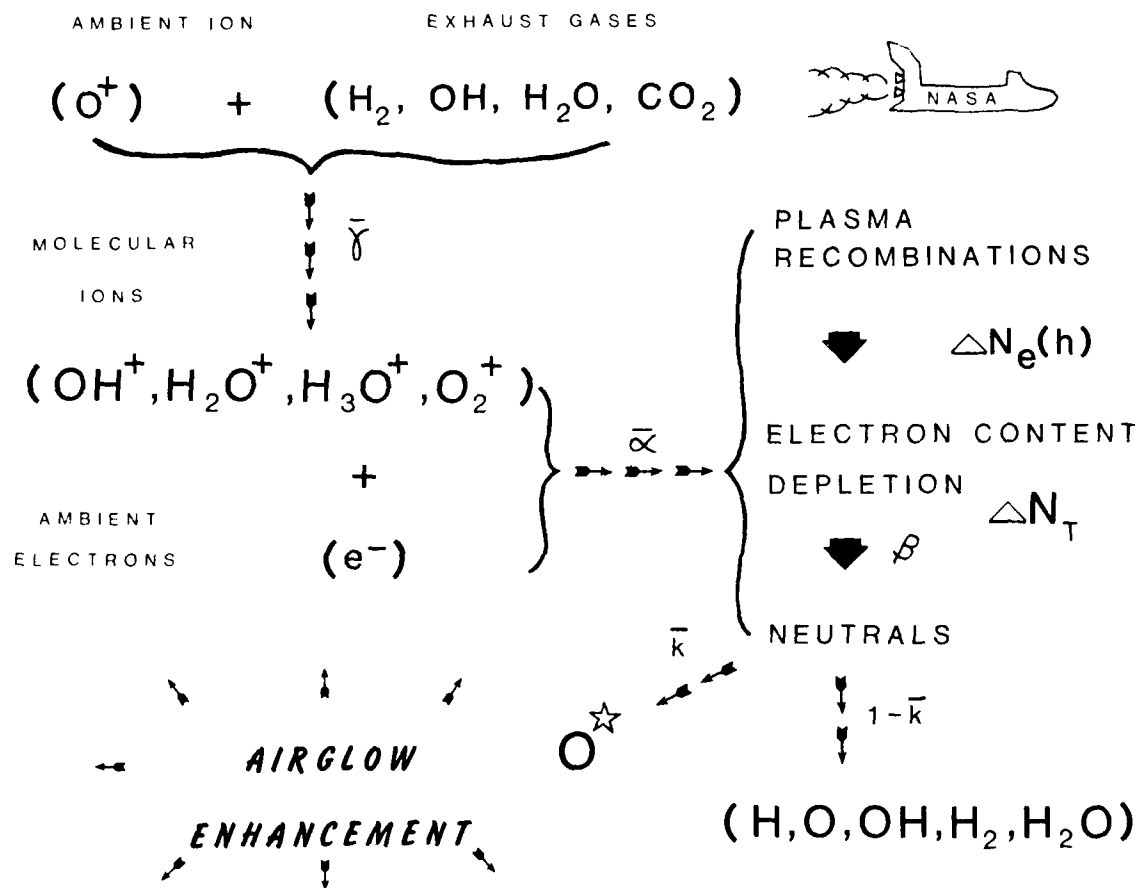
FIGURE 7. Theoretical estimates of 6300 Å airglow from equation (4); see text.

The delayed t_{max} and slow return to ambient 6300 Å levels shown in Figure 2 must result from processes not considered in the simple formulation leading to equation (4). The 110 second lifetime for O^* is sufficiently long to allow for $[O^*]_T$ to change by diffusion into and out of the line of sight monitored by the photometer. Moreover, the diffusion of ambient O^+ into the molecular rich hole at later times could produce additional O^* that are not detected by the Faraday technique (note that $dN_T/dt \simeq 0$ from 11:00 - 11:15 U.T. in Figure 2, and thus further plasma recombinations could be masked by a matching plasma influx.) In relating the production of $[O^*]_T$ to $-k$ (N_T/dt) in equation (2), there is an assumption that each recombination has the potential of producing an O^*; Anderson and Bernhardt (1978) have shown that in a dense environment of H_2 (as occurs at early times), molecular ions such as H_2O^+ are formed that recombine very rapidly $(H_3O^+ + e^- \rightarrow H_2O + H)$ but do not yield $O(^1D)$ states. To the extent that this occurs, the production of $[O^*]_T$ in equation (2) is overestimated at early times, and thus a correction in the proper sense is obtained.

The assumption of a high efficiency (k = 1-1.3) for $O(^1D)$ production per recombination of O_2^+ (Roble et al., 1976; Hays et al., 1978) seems at odds with the low column-average k values depicted in Figure 7. This suggests that k is a function of relative composition, and therefore of time and space. Since the yield of O^* is high from O_2^+, the CO_2 component of the plume must have been a minor contributor to the observed TEC decrease. In comparison to CO_2, the other exhaust gases have faster reaction rates with O^+, greater diffusion coefficients and a combined abundance $\sim 3\frac{1}{2}$ times the CO_2 in the plume. Thus, while H_2 and H_2O are very efficient hole-makers, they must produce O^* at relatively low efficiencies, while the opposite case seems to occur for CO_2.

A more extensive examination of this and a similar Atlas-F event using networks of TEC and 6300 Å observations will be described in a later paper. The single-site data presented here were used to illustrate the potential benefits to be gained by active space plasma experiments in the ionospheric domain. Figure 8 contains a summary (few of such work.

IONOSPHERIC HOLES AND 6300 Å AIRGLOW

AMBIENT ION   EXHAUST GASES

$$(O^+) \quad + \quad (H_2, OH, H_2O, CO_2)$$

NASA

MOLECULAR IONS $\bar{\gamma}$

PLASMA RECOMBINATIONS

$\triangle N_e(h)$

$$(OH^+, H_2O^+, H_3O^+, O_2^+)$$

$+$

AMBIENT ELECTRONS (e^-)

$\bar{\alpha}$

ELECTRON CONTENT DEPLETION $\triangle N_T$

β

$\bar{k}$ NEUTRALS

$O^{☆}$ $1-\bar{k}$

AIRGLOW ENHANCEMENT

$$(H, O, OH, H_2, H_2O)$$

--Relation between column-integrated quantities--

$$E_T(t) = \frac{A_{6300}\, \bar{k}\, \beta\, \triangle N_T}{A_T + \bar{Q}_T - \beta}\left(e^{-\beta t} - e^{-(A_T + \bar{Q}_T)\cdot t}\right)$$

Use observed (E_T, N_T) to solve for $(\bar{k}, Q_T)$

FIGURE 8.   Ionospheric modifications for laboratory-in-space research.

REFERENCES

Anderson, D.N. and P.A. Bernhardt, Modeling the effects of an H_2 gas release on the equatorial ionosphere, J. Geophys. Res., 83, 4777, 1978.

Bernhardt, P.A., High-altitude gas releases: transition from collisionless flow to diffusive flow in a nonuniform atmosphere, J. Geophys. Res., 84, 4341, 1979.

Bernhardt, P.A., C.G. Park, and P.M. Banks, Depletion of the F2 region ionosphere and the protonosphere by the release of molecular hydrogen, Geophys. Res. Lett., 2, 341, 1975.

CIRA, Cospar International Reference Atmosphere, Akademic-Verlag, Berlin, 1972.

Forbes, J.M., Yield of O (^{1}D) by dissociative recombination of $O_2{}^+$ from night airglow observations, J. Atmosph. Terr. Phys., 32, 1901, 1970.

Hays, P.B., D.W. Rusch, R.G. Roble, and J.C.G. Walker, The OI (6300 Å) airglow, Rev. Geophys. Space Sci., 16, 225, 1978.

Hudson, R.D. and E.I. Reed (Eds.), the Stratosphere: Present and Future, NASA RP-1049, Washington, DC, 1979.

Kofsky, I.L., D.P. Villannui and E.R. Huppi, Preliminary report on aircraft measurements of optical/IR afterglows from a major ionosphere perturbation, Proc. Workshop/Symposium on the preliminary evaluation of the ionospheric disturbances associated with the HEAO-C launch, with applications to the SPS environmental assessment, M.Mendillo (editor), Conf. Rept. # 7911108, U.S. Dept. of Energy, August 1980.

Mendillo, M., The effect of rocket launches on the ionosphere, Adv. Space Res., 1, 275, 1981.

Mendillo, M., D. Rote and P. Bernhardt, Preliminary report on the HEAO hole in the ionosphere, EOS, 61, 529, 1980.

Mendillo, M. and J.M. Forbes, Artificially created holes in the ionosphere, J. Geophys. Res., 83, 151, 1978.

Mendillo, M., G.S. Hawkins and J.A. Klobuchar, A sudden vanishing of the ionospheric F region due to the launch of Skylab, J. Geophys. Res., 80, 2217, 1975.

Roble, R.G., J.F. Noxon and J.V. Evans, The intensity variation of the atomic oxygen red line during morning and evening twilight on 9-10 April 1969, Planet. Space Sci., 24, 327, 1976.

Schunk, R.W., On the dispersal of artificially-injected gases in the night-time atmosphere. Planet. Space Sci., 26, 605, 1978.

Stone, S.N. abd J. Zinn, Quick look summary of Atlas-Centaur airglow observations, Proc. Workshop/Symposium on the preliminary evaluation of the ionospheric disturbances associated with the HEAO-C launch, with applications to the SPS environmental assessment, M.Mendillo (editor), Conf. Rept. # 7911108, U.S. Dept. of Energy, August 1980.

Titheridge, J.E., Determination of ionospheric electron content from the Faraday rotation of geostationary satellite signals, Planet Space Sci., 20, 353, 1972.

Zinn, J. and C.D. Sutherland, Effects of rocket exhaust products in the thermosphere and ionosphere, Space Solar Power Rev., 1, 109, 1980.

END